

High-quality Thermal Gibbs Sampling with Quantum Annealing Hardware

Jon Nelson,¹ Marc Vuffray,² Andrey Y. Lokhov,² Tameem Albash,^{3,4} and Carleton Coffrin¹

¹*Advanced Network Science Initiative, Los Alamos National Laboratory, Los Alamos, NM, USA*

²*Theoretical Division, Los Alamos National Laboratory, Los Alamos, NM, USA*

³*Department of Electrical and Computer Engineering,
University of New Mexico, Albuquerque, NM, USA*

⁴*Department of Physics and Astronomy and Center for Quantum Information and Control,
University of New Mexico, Albuquerque, NM, USA*

Quantum Annealing (QA) was originally intended for accelerating the solution of combinatorial optimization tasks that have natural encodings as Ising models. However, recent experiments on QA hardware platforms have demonstrated that, in the operating regime corresponding to weak interactions, the QA hardware behaves like a noisy Gibbs sampler at a hardware-specific effective temperature. This work builds on those insights and identifies a class of small hardware-native Ising models that are robust to noise effects and proposes a novel procedure for executing these models on QA hardware to maximize Gibbs sampling performance. Experimental results indicate that the proposed protocol results in high-quality Gibbs samples from a hardware-specific effective temperature and that the QA annealing time can be used to adjust the effective temperature of the output distribution. The procedure proposed in this work provides a new approach to using QA hardware for Ising model sampling presenting potential new opportunities for applications in machine learning and physics simulation.

I. INTRODUCTION

The computational task of sampling – that is producing independent configurations of random variables from a given distribution – is believed to be among the most challenging computational problems. In particular, many sampling tasks cannot be performed in polynomial time, unless strong and widely accepted conjectures in approximation theory are refuted [1–3]. Consequently, state-of-the-art algorithms for general purpose sampling are based on Monte Carlo methods that require significant computing resources to sample from distributions of practical interest.

Gibbs distributions, i.e., distributions with the form $P(\sigma) \propto \exp(-\beta H(\sigma))$, have close ties to modeling many physical systems as they capture the equilibrium configurations that matter takes at a given inverse temperature β [4]. It has also been observed that Gibbs distributions provide a powerful foundation for building machine learning models and optimization algorithms [5, 6]. However, the computational challenge of sampling from these distributions is often prohibitive for practical applications of machine learning and optimization. It has been observed that a variety of the emerging analog computing devices, including those based on optical [7] and quantum [8] technologies, can be used as fast Gibbs samplers because of the natural connection between probabilistic physical systems and state sampling. The emergence of these novel computing devices has the potential for a dramatic impact on state-of-the-art approaches for physics simulation, machine learning and optimization.

From its inception, Quantum Annealing [9–12] (QA) has been designed for solving optimization tasks and not sampling tasks. However, in practice, various non-ideal properties of QA hardware platforms lead to outputs that are reminiscent of thermal Gibbs distributions [13–16].

Recent experiments have demonstrated that, in the operating regime corresponding to weak interactions, QA hardware behaves like a *noisy Gibbs sampler* [17] at a hardware-specific effective temperature, that is, a sampler from a mixture of Gibbs distributions with fluctuating parameters caused by noise. Furthermore, it was shown in [17] that samples from this noisy mixture of distributions is indistinguishable from a single Gibbs distribution with spurious additions to interaction structure of the programmed model. In applications where sampling from a specific Gibbs distribution is required, this distortion of the model parameters may present an undesirable feature because of this mismatch in model structure.

Building on the insights of [17], this work demonstrates that it is possible to leverage QA hardware to perform high-quality Gibbs sampling from some types of input models. In particular, we identify a class of hardware-native Ising models where the D-Wave 2000Q platform consistently produces samples with a total variation less than 5% from a desired target Gibbs distribution. We also show that changing the annealing time enables the QA hardware to sample from a range of inverse temperatures between 1.9 and 5.1, which is an essential feature in a variety of applications. This work leverages the combination of three novel insights to achieve high-quality Gibbs sampling on the QA hardware: (1) it focuses on the hardware-native Ising models that are resilient to the hardware’s noise; (2) the input models are re-scaled to avoid distortions caused by the transverse field in the computational model; and (3) both the annealing time and the model’s energy scale are leveraged to control the effective temperature of the target distribution. To the best of our knowledge, the approach outlined in this paper provides the first prescriptive procedure for conducting high-quality Ising model Gibbs sampling on QA hardware without the need to tune the input model or

perform post-processing to correct for distorted output distributions. If required, both of these procedures can be leveraged to further improve the results presented in this work, as done in [13, 18, 19].

This work begins by reviewing the computational model of quantum annealing and previous works exploring sampling applications in Section II. Building on these previous works, a new approach for conducting high-quality thermal Gibbs sampling is proposed in Section III and evaluated on quantum annealing hardware. Section IV explores theoretical models to provide insights into the mechanisms that under-pin the proposed sampling approach and Section V concludes with a discussion of future directions.

II. PROBLEM FORMULATION & RELATED WORK

The foundational physical system of interest to this work is the Ising model, a class of graphical models where the nodes, V , represent classical spins (i.e., $\sigma_i \in \{-1, 1\} \forall i \in V$), and the edges, $E \subseteq N \times N$, represent pairwise spin interactions. A local field $h_i \forall i \in V$ is specified for each spin and an interaction strength $J_{ij} \forall i, j \in E$ is specified for each edge. The energy of a given spin configuration is given by the Hamiltonian:

$$H_{\text{Ising}}(\sigma) = - \sum_{i,j \in E} J_{ij} \sigma_i \sigma_j - \sum_{i \in V} h_i \sigma_i . \quad (1)$$

This Ising model is widely used to encode challenging computational problems arising in the study of magnetic materials, machine learning, and optimization [20–23]. The particular computational task of interest to this work is to produce i.i.d. samples σ from the Gibbs distribution associated with the Ising model at the inverse temperature¹ α , that is,

$$\mu(\sigma) \propto \exp(-\alpha H_{\text{Ising}}(\sigma)) . \quad (2)$$

Throughout this work, we assume that the parameters J, h are in the range of -1 to 1 , to provide a consistent scaling for α . Given the computational challenge of Ising model sampling at finite temperature, our objective is to leverage QA hardware to conduct this task.

A. A Brief Review of Quantum Annealing

The central idea of quantum annealing is to use the transverse field Ising model combined with an annealing

process to find the low-energy configurations of a classical Ising model. The elementary unit of this model is a qubit $i \in V$ described by the standard vector of Pauli matrices $\{\hat{\sigma}^x, \hat{\sigma}^y, \hat{\sigma}^z\}$ along the three spatial directions $\{x, y, z\}$. The hardware platform provides a programmable Ising model Hamiltonian on the z -axis [9],

$$\hat{H}_{\text{Ising}} = - \sum_{ij \in E} J_{ij} \hat{\sigma}_i^z \hat{\sigma}_j^z - \sum_{i \in V} h_i \hat{\sigma}_i^z, \quad (3)$$

which encodes the Ising energy function (1) with a one-to-one mapping of qubits to Ising spins. Note, that the eigenvalues of the Ising Hamiltonian operator are in bijection with the 2^N possible assignments of the classical Ising model from Eq. (1). The quantum annealing protocol strives to find the low-energy assignments to a user-specified \hat{H}_{Ising} model by conducting an analog interpolation process of the following transverse field Ising model Hamiltonian:

$$\hat{H}(s) = -A(s) \sum_{i \in V} \hat{\sigma}_i^x + B(s) \hat{H}_{\text{Ising}}. \quad (4)$$

The interpolation process starts with $s = 0$ and ends with $s = 1$. The two interpolation functions $A(s)$ and $B(s)$ are designed such that $A(0) \gg B(0)$ and $A(1) \ll B(1)$, that is, starting with a Hamiltonian dominated by $-\sum_{i \in V} \hat{\sigma}_i^x$ and slowly transitioning to a Hamiltonian dominated by \hat{H}_{Ising} . In the closed system setting and when this transition process is sufficiently slow, quantum annealing will find the ground states of \hat{H}_{Ising} , and therefore minimizing configurations of H_{Ising} , with high probability [24–28]. To that end, the length of the annealing process t (in microseconds) is a user controllable parameter. The outcome of the quantum annealing process is specified by the binary string σ , where each element σ_i takes a value $+1$ or -1 and corresponds to the observation of the spin projection of qubit i in the computational basis denoted by z .

B. Quantum Annealing and Sampling

Given the energy minimizing nature of quantum annealing, it is not immediately clear how it may be applied to the sampling task posed in (2). It is reasonable to postulate that an adiabatic system would behave similarly to Gibbs sampling at the zero temperature limit (i.e., $\alpha = \infty$), that is drawing i.i.d. samples from the ground states of H_{Ising} . Interestingly, this is not usually the case as the transverse field component of the Hamiltonian, $\hat{\sigma}_i^x$, induces biases in the annealing process to prefer some ground states over others [29–32]. Nevertheless, protocols have been proposed to help increase the fairness of ground state sampling using quantum annealing [33, 34]. In contrast to previous works, this work is concerned with sampling from thermal distributions (i.e.,

¹ Throughout this work, α is used to denote the energy scale of a Gibbs distribution and β is used to indicate the effective inverse temperature of the quantum annealer.

$\alpha < \infty$), which requires accurate sampling at all of the energy levels of H_{Ising} , presenting a formidable challenge in model accuracy.

Real-world QA hardware is an open quantum system that is subject to a wide variety of non-ideal properties, including thermal excitations and relaxations that impact the results of the computation [35–37]. In this regard, the relevant adiabatic theorem is the open system adiabatic theorem [38–40]: if the dynamics is governed by a master equation of Lindblad form [41] and if the annealing is done sufficiently slowly, the system will converge with high probability to the steady state of the dynamics. This result is promising because, for certain master equations, the thermal Gibbs state is the steady-state solution [42, 43].

In addition to the fundamental impacts of open quantum systems, the D-Wave hardware documentation highlights five other sources of deviations from ideal system operations called *integrated control errors* (ICE) [44], which include: background susceptibility; flux noise; Digital-to-Analog Conversion quantization; Input/Output system effects; and variable scale across qubits. Consequently, it has long been observed that output distributions of the QA hardware produced by D-Wave Systems are reminiscent of a Gibbs distribution of the input Hamiltonian H_{Ising} [13–16, 18] with a hardware-specific effective temperature of $\beta \approx 10$ [17, 45]. The prevailing interpretation of the hardware’s output distribution is the *Freeze Out* model, which proposes that the output reflects a quantum Gibbs distribution occurring at an input-dependent point towards the end of the annealing process where some small amount of $\hat{\sigma}_i^x$ remains [46]. This model has been notably successful for training quantum machine learning models [47, 48] and generating statistics for quantum Gibbs distributions [49–51]. However, these quantum Gibbs distributions are inaccurate when targeting a desired classical Gibbs distribution for sampling applications [6, 18, 52, 53]. The recent insight from [17] is that when this hardware is operated at a low-energy scale (i.e., $|J|, |h| \leq 0.050$) it behaves as a thermalized classical Gibbs sampler from H_{Ising} but suffers from a notable amount of distortion from instantaneous noise in the local field parameters, h , on the order of 0.036 [45, 54], resulting in so-called noisy Gibbs samples.

Inspired by the classical Gibbs sampling insights of [17], this work demonstrates that there exists a class of Ising Hamiltonians where D-Wave’s 2000Q hardware produces high-quality Gibbs samples, with minimal distortions from noise or transverse fields. In particular, we consider the class of H_{Ising} with $J, h \in \{-1, 0, 1\}$, $|V| \leq 16$ that are representable on the D-Wave 2000Q hardware graph. The primary insight of this work is to operate the QA hardware at an energy scale, α_{in} , that is large enough to be noise-resilient but small enough to avoid the degeneracy breaking properties of the transverse field. It is not guaranteed that such a ‘sweet-spot’ exists but this work demonstrates that the range

of $0.2 \leq \alpha_{in} \leq 0.4$ on the platform considered achieves the desired properties. A discussion at the conclusion of the paper provides a qualitative study postulating why a sweet-spot occurs at this particular energy scale. Additionally, this work shows that in the proposed energy scale the annealing time has a consistent effect of tuning the effective temperature (i.e., α) of the Gibbs samples generated by the hardware. Combined these observations present new opportunities for leveraging QA hardware for conducting the Ising model sampling task described by (2).

III. EXPLORING GIBBS SAMPLING WITH QUANTUM ANNEALING HARDWARE

This work is concerned with the following four parameters: H_{Ising} , the Ising model that one would like to sample from (restricted to $J, h \in \{-1, 0, 1\}$); $\alpha_{in} \in [0, 1]$, a scaling factor that will be used when programming the QA hardware; t , the annealing time of the QA protocol; and $\alpha_{out} \in [0, \alpha_{\text{max}}]$, a scaling factor of the distribution output by the QA hardware. Given H_{Ising} , the QA hardware is programmed with the re-scaled model $H_{\text{Ising}}^{in} = \alpha_{in} H_{\text{Ising}}$ and executed with an annealing time t . The empirical distribution output by the hardware ν is then compared to Gibbs distributions of H_{Ising} at different effective temperatures, i.e., $\mu(\alpha, \sigma) \propto \exp(-\alpha H_{\text{Ising}}(\sigma))$. We define α_{out} as,

$$\alpha_{out} = \operatorname{argmin}_{\alpha} \operatorname{TV}(\nu, \mu(\alpha)), \quad (5)$$

that is, the effective temperature of the closest Gibbs distribution of H_{Ising} to the results output by the hardware, using total variation distance (TV) as the measure of closeness. Details of the total variation metric are provided in Appendix A. The remainder of this section explores how changes in the α_{in} and t parameters impact the output distribution of the D-Wave 2000Q Quantum Annealer located at Los Alamos National Laboratory, known as DW_2000Q_LANL. The unexpected finding is that there exists range of α_{in} values where the QA hardware is a high-quality Gibbs sampler.

A. Experiment Design

1. Ising Model Selection

Given the challenges of sampling from embedded Ising models [52], this work focuses exclusively on H_{Ising} Hamiltonians that have native representation in the QA hardware. In particular, the D-Wave 2000Q system implements a C_{16} chimera graph [55], which consists of a 16×16 grid of unit cells each containing 8 qubits (4 horizontal and 4 vertical). In each unit cell, every horizontal qubit is connected to every vertical qubit through couplers and various qubits in adjacent unit cells are also

connected through couplers. The coupling strength J_{ij} between qubits i and j can be programmed to values in the continuous range $[-1, 1]$, and the local fields h_i can be programmed to values in the range $[-2, 2]$.

In selecting the Ising models for testing Gibbs sampling with QA, we strive to design models that exhibit a variety of sampling difficulties. Previous works have highlighted that QA will prefer some degenerate ground states over others as a result of residual effects from the annealing process [29–32]. As ground states are the most heavily weighted states in the low-temperature Gibbs distribution, these asymmetries introduce significant sampling errors. In this work, we elicit this effect by constructing a set of 13 models with ground-state degeneracies ranging from 1 to 38 to capture both easy and challenging instances to sample from with a quantum annealer.

In particular, this work considers seven *GSD* (ground-state degeneracy) cases with degeneracy values of 2, 4, 6, 8, 10, 24, and 38, without local fields, and six additional *GSD-F* models with 1, 2, 3, 4, 5, and 6 ground state degeneracies including local fields. Note that the *GSD-F* models tend to have lower degeneracy because the inclusion of the fields breaks symmetries within energy levels. The specific instances are referred to as *GSD-#* and *GSD-F-#* where the *#* indicates the amount of ground state degeneracy. The Hamiltonian’s of each instance and a discussion of how they were designed is provided in Appendix B.

2. Quantum Annealing Data Collection

For each of the *GSD* models, H_{Ising} , a family of hardware inputs is considered by sweeping α_{in} between 0.0 and 1.0 with step size of 0.0125 below 0.1, 0.025 between 0.1 and 0.5, and 0.1 above 0.5. The increased step size for low scales is helpful as the output statistics tend to be more sensitive to α_{in} in this regime. For each of these models and scales, 10^6 samples are collected from the QA hardware. After every 100 samples, a gauge transform is applied in order to mitigate the effects of bias. For each gauge transformation, a randomly generated vector $\vec{a} \in \{-1, 1\}^V$ is used to redefine the Ising parameters via $h_i \rightarrow a_i h_i, J_{ij} \rightarrow a_i a_j J_{ij}$. This transformation preserves the energy eigenvalues of $H(s)$, but it relabels the spin configurations σ by $\sigma_i \rightarrow a_i \sigma_i$. Using gauge transformations is a well-known technique for eliminating these field biases, which can add additional unwanted asymmetries [17, 56, 57]. After the samples have been collected, the empirical probability of each state is recorded. This data collection process is repeated for annealing times t of 1 μs , 5 μs , 25 μs , and 125 μs .

3. Estimating the Effective Output Temperature

As discussed at the beginning of this section, we would like to identify the closest Gibbs distribution of H_{Ising} to the empirical distribution output by the QA hardware, i.e., (5). However, the exact solution of the optimization task posed by (5) presents a significant computational challenge because of difficulties in computing candidate Gibbs distributions. The primary reason that this work has focused on the small-scale Ising models with only 16 spins is to make this optimization task computationally tractable. In this work, the optimization problem (5) is solved by a brute-force calculation of the total variation for a discrete set of α values. The α values are determined by calculating an optimistic estimate for α_{max} and then scaling this value by the same step sizes that are used for α_{in} . The α_{max} value is calculated by executing the QASA protocol proposed in [45] on each of the relevant spins and taking the average of the spin-by-spin effective temperatures recovered by that protocol. Therefore, the minimum of the range is 0.0 and the maximum is α_{max} . The α value from this discrete set that achieves the minimum total variation between the quantum annealing data and the Gibbs distribution is selected as α_{out} . In the results, we observe that $\alpha_{out} \ll \alpha_{\text{max}}$ indicating that α_{max} is a sufficiently optimistic value for this brute-force optimization procedure in practice.

4. Bounding Finite Sampling Performance

Because the empirical distribution produced by the QA hardware is calculated from finite samples, there is an unavoidable error caused by finite sampling (details are discussed in Appendix A). To understand the impact of this finite sampling error, a lower bound is calculated by a simulation procedure that generates 10^6 samples from the selected α_{out} Gibbs distribution and calculates the total variation between this empirical distribution and the exact distribution. Because the samples are generated from a known source distribution, the only source of error is a result of finite sampling. Therefore, this value represents the best total variation that is achievable given the number of samples that were used in these experiments 10^6 . This lower bound is included in the result figures to provide a measure of the total variation error that can be attributed solely to the limitations of finite sampling. In this work we find that this sampling issue is only significant when the input scale is low ($\alpha_{in} < 0.1$) as this regime reflects a distribution that is close to uniform and the probability mass is spread out among exponentially many states. The presence of errors caused by finite sampling motivates our use of a large number of samples (i.e., 10^6 per data point) and provides an explanation for some of the consistent features in the results that are observed in the low α_{in} regime.

B. Experiment Results

1. A Typical GSD Model

We begin by presenting detailed results on a characteristic GSD model and then provide a summary of the results across the complete collection of models. The total variation results for the GSD-6 model are presented in Figure 1. As the value of α_{in} is increased, the results show an up-down-up shape in the TV metric. At very low $\alpha_{in} < 0.01$, the TV value is limited by finite sampling effects. As α_{in} is increased, it quickly deviates from the family of H_{Ising} Gibbs distributions and gradually becomes more Gibbs-like. At some point, while increasing α_{in} , a minimum TV value is reached and it begins to increase monotonically until the maximum α_{in} value. This up-down-up trend is replicated across a variety of the models considered in this work and plausible causes for it are discussed in Section IV. The central observation of this analysis is that there is a band of α_{in} between approximately 0.2 and 0.4, where the QA hardware’s output distribution deviates from the target Gibbs distribution by less than 5% in total variation, which we designate as *high-quality*. Outside of this particular range of α_{in} , the total variation increases considerably, showing how the QA hardware’s distribution dramatically shifts away from the family of H_{Ising} Gibbs distributions. Interestingly, there does not seem to be any significant dependence of the total variation on annealing time (i.e., each of the colored points in Figure 1 follow similar trends). These results suggest that this middle regime of α_{in} is favorable for using QA hardware as a Gibbs sampler at each of the annealing times considered. Similar results on all of the GSD instances are provided in Appendix C.

The results from Figure 1 suggest there are operating regimes where the QA hardware’s is an accurate Gibbs sampler; however, the effective temperature (i.e. α_{out}) of the that distribution is not presented. Figure 2 explores this point by presenting the α_{out} values that were found for each of the high-quality input configurations considered (i.e., $0.2 \leq \alpha_{in} \leq 0.4$). Given the prevailing theories of how QA hardware operates [45, 46], one expects that increasing the energy scale of the input α_{in} or the annealing time will increase the effective temperature of the output distribution, α_{out} . Indeed, that trend is observed in Figure 2, where the recovered α_{out} values increase monotonically (or nearly so) with both α_{in} and annealing time. This monotonicity is a particularly useful result as it suggest a simple procedure for tuning the effective temperature of the distribution output by the QA hardware platform, which is an essential feature for most practical sampling applications.

Generating Gibbs samples in the α_{out} range of from 1.85 to 5.16 as shown in Figure 2 is an encouraging result as the critical points separating high- and low-temperature regimes of Ising spin glasses on lattices and random graphs typically occurs for values of $\alpha_{out} < 1.0$ [22]. Sampling from these low-temperature regimes is

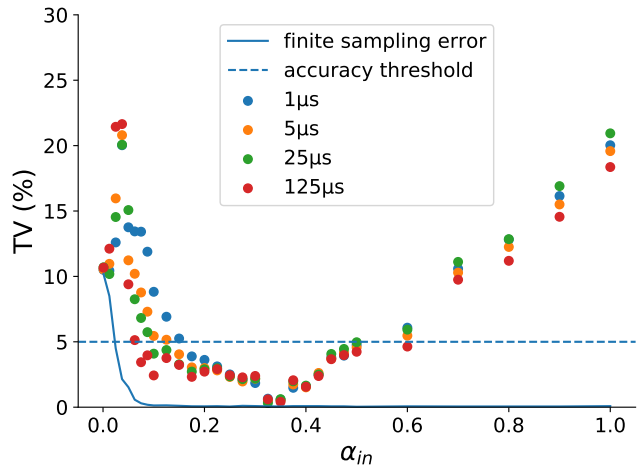


FIG. 1: Total variation between QA hardware output distribution for various scalings α_{in} and target Gibbs distribution with estimated α_{out} on the GSD-6 Hamiltonian. This model contains 16 spins and six ground states. Experiment is repeated for annealing times of $1 \mu s$ (blue), $5 \mu s$ (orange), $25 \mu s$ (green), and $125 \mu s$ (red). Finite sampling lower bound is indicated by blue curve. The *accuracy threshold* indicates the statistical requirement to be considered a high-quality Gibbs sampler in this work. The surprising finding is the band of α_{in} between approximately 0.2 and 0.4 where the hardware output does conform to a Gibbs distribution of the input Hamiltonian.

known to present significant computational challenges for classical algorithms, giving hope that QA hardware may be able to provide a performance enhancement on these tasks. However, additional study is needed to determine if the results presented here can generalize to larger system sizes and to temperatures below the critical point of natively representable Ising spin glasses [58].

2. Summary of the GSD Models

To test if the observations on the GSD-6 instance generalize to a broader collection of models, we repeated the previous experiment on all 13 of the GSD models proposed in this work, seven GRD and six GSD-F cases. Figure 3 displays the minimum total variation with respect to the ideal Gibbs distribution for each scale of α_{in} and for each model. Only the $1 \mu s$ data is presented, but results with other annealing times are available in Appendix C. Although one can observe a variety of distinct features across these instances, the encouraging finding is that the range of α_{in} within 0.2 and 0.4 consistently yields statistics with low total variation values, suggesting the observations on the GSD-6 model do generalize to a broader class of models. In particular, $\alpha_{in} \approx 0.3$ achieves a low total variation for nearly all of the models

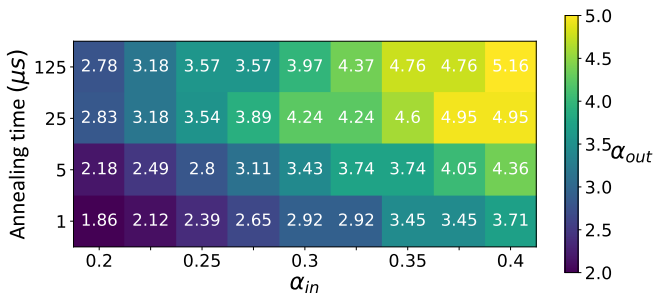


FIG. 2: The values of α_{out} recovered by operating the QA hardware at different values of α_{in} and annealing times in the high-quality regime identified in Figure 1 for the GSD-6 Hamiltonian. Encouragingly, α_{out} increases monotonically (or nearly so) with both α_{in} and annealing time, allowing the hardware generate distributions at different effective temperatures, which is an essential feature for practical applications.

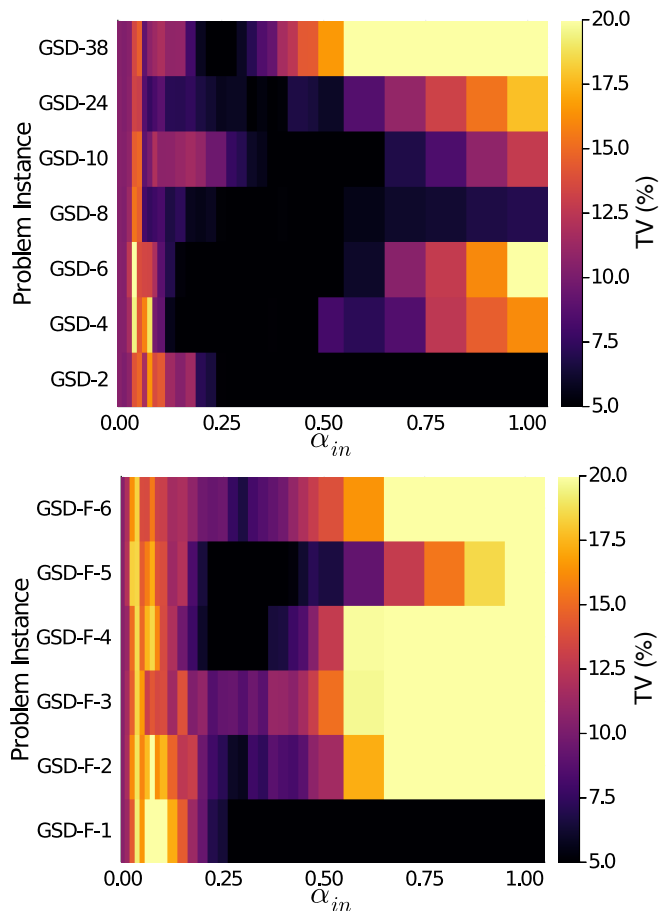


FIG. 3: Total variation between QA hardware output distribution for various scalings α_{in} and target Gibbs distribution with estimated α_{out} on the all GSD instances (top) and GSD-F instances bottom. A consistent high-quality Gibbs sampling band is observed for $0.2 \leq \alpha_{in} \leq 0.4$, with $\alpha_{in} \approx 0.3$ achieving a low total variation for nearly all of the GSD models.

considered.

It is important to briefly discuss the GSD-2 and GSD-F-1 models, as these are the only ones that do not follow the up-down-up trajectory shown in Figure 1. In these cases, the total variation is high for low α_{in} and then drops below 5% for α_{in} greater than 0.2 as expected. However, the total variation remains low even for α_{in} greater than 0.4. This result is because when α_{in} is large, the probability distribution is highly concentrated in the ground states and these instances do not exhibit ground state degeneracy breaking. As there is only one ground state in the GSD-F case and two symmetrical ground states in the GSD case, the sampling task is relatively easy and effectively reduces to a ground state identification task. The QA hardware achieves low TV in these cases by simply outputting the ground states with high probability. Although one can consider these two cases to represent *easy* sampling tasks, we include them to highlight the increased challenge that instances with more ground state degeneracy pose to using QA for sampling applications.

The results from Figure 3 indicate that the proposed high-quality Gibbs sampling regime generalizes to a variety of Ising models; however, the stability of the effective temperatures (i.e., α_{out}) of those distributions is an important question. Table I provides a summary of this information by presenting the minimum and maximum α_{out} values that can be achieved on each model by varying both α_{in} and the annealing time (see Appendix D for more detailed information). Although there is some variability in the largest α_{out} values, the results indicate that the range of effective temperatures output by the hardware remains relatively stable and the hardware is suitable for sampling from all models between 1.85 and 3.97. These results also suggest that the observations on the GSD-6 model generalizes to a broader class of models.

IV. DISCUSSION

Using quantum annealing for Gibbs sampling has been proposed as early as 2010, [13]. Since then, several studies have indicated that the output distribution of a quantum annealer does not sample from the input Hamiltonian's Gibbs distribution [6, 18, 31, 32]. However, many of these works use an input scaling that is outside of the range identified by this work and are therefore subject to the distortions that we see in Figures 1 and 3. These figures show that if α_{in} is too small (< 0.2) or too large (> 0.4) then QA hardware's output distribution will differ greatly from that of a corresponding Gibbs distribution. Additionally, observing that the QA operating protocol proposed by this work yields high-quality Gibbs samples in a variety of Ising models suggests a systematic phenomenon that produces this behavior.

To investigate what might account for the distortions in these Gibbs distributions and the unique features that

Instance	min α_{out}	max α_{out}
GSD-2	1.32	3.97
GSD-4	1.85	4.95
GSD-6	1.85	5.16
GSD-8	1.59	4.37
GSD-10	1.32	4.76
GSD-24	1.59	4.58
GSD-38	1.59	4.76
GSD-F-1	1.32	3.97
GSD-F-2	1.32	4.37
GSD-F-3	1.59	4.37
GSD-F-4	1.59	4.58
GSD-F-5	1.59	4.76
GSD-F-6	1.59	4.37

TABLE I: A summary of the smallest and largest α_{out} values recovered by operating the QA hardware at different values of α_{in} and annealing times in the high-quality regime across all GSD models. Although there is some variation in the largest α_{out} values, the QA hardware has a fairly consistent behavior across the GSD models and suggests that samples can be generated effectively in the range of effective temperatures from at least 1.85 to 3.97 for a variety of Hamiltonians.

occur in the $0.2 \leq \alpha_{in} \leq 0.4$ range, we conduct a detailed study of the output statistics of a very small Ising Hamiltonian, i.e., a three-spin Ising chain. With such a small system, we are able to create a theoretical model that reproduces the experimental data. This theoretical model suggests local field noise and residual transverse field effects as potential explanations for the observed distortions. The theoretical model found that the three-spin system sampled from an Ising Hamiltonian with extraneous couplings when α_{in} was in the low- or high-scaling regime. Only when α_{in} remained in the range identified by this work did the system produce the desired Gibbs distribution. This result provides additional evidence that this restricted scaling regime is optimal for conducting Gibbs sampling with QA hardware.

A. Three-spin Ising Chain Statistics

In this experiment, three spins denoted by σ_1 , σ_2 , and σ_3 are linked together in a ferromagnetic chain with σ_1 coupled to σ_2 and σ_2 coupled to σ_3 as shown in Figure 4. Notice that σ_3 is not coupled to σ_1 . Formally, the input Hamiltonian is defined as follows:

$$H_{\text{Ising}} = -J_{in}(\hat{\sigma}_1^z \hat{\sigma}_2^z + \hat{\sigma}_2^z \hat{\sigma}_3^z), \quad (6)$$

where J_{in} is the value of the coupling. J_{in} is swept between 0.0 and 1.0 with step-sizes matching the discretiza-

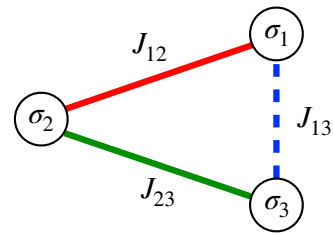


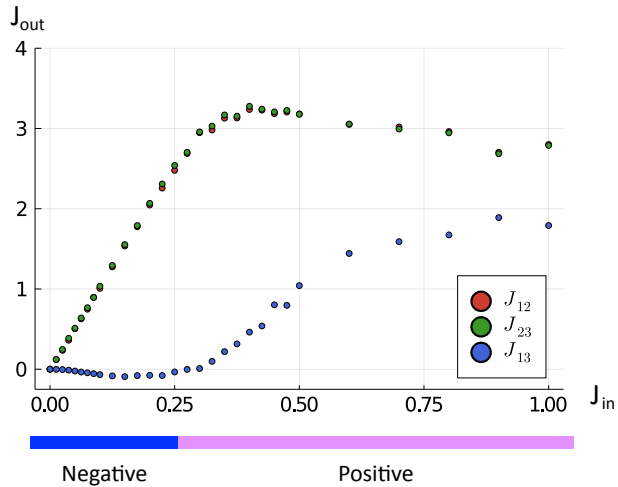
FIG. 4: Diagram of three-spin Ising chain experiment. Solid lines for J_{12} and J_{23} indicate couplings that are programmed in the input Hamiltonian. Dashed line for J_{13} indicates that this coupling is not programmed in the input Hamiltonian even though it is reconstructed from the output statistics and is thus a “spurious coupling.”

tion of α_{in} from the 16-spin experiments.² For each value of J_{in} , 5×10^6 samples are collected from the QA hardware and the output statistics are recorded. Once again, in order to mitigate bias a spin-reversal transform is applied after every 100 samples.

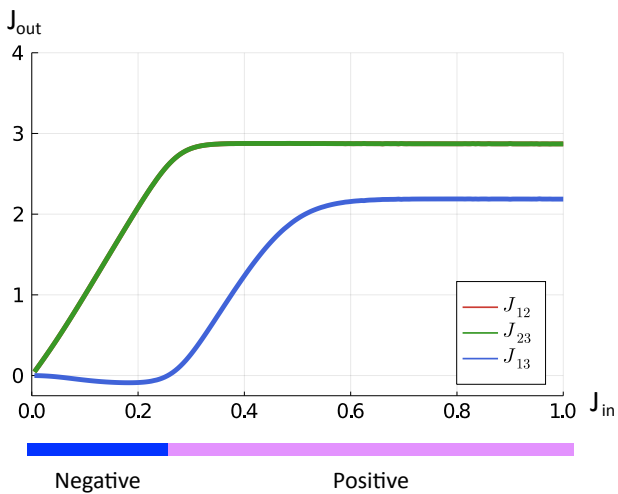
The output distribution is analyzed by solving the inverse-Ising problem using the Interaction screening estimation algorithm [22, 59]. This algorithm takes the empirical distribution produced by the hardware and estimates the Ising Hamiltonian that most likely produced the given output statistics. The estimated values for each of the couplings are denoted as J_{out} and more specifically as J_{12} , J_{23} , and J_{13} to indicate the specific edge in the three-spin chain. These estimated values are compared to the corresponding input values J_{in} in Figure 5a. This procedure provides an understanding of the effective Hamiltonian output by the QA hardware, which may differ from the Ising Hamiltonian that has been programmed. The entire protocol is repeated for annealing times of $1 \mu s$, $5 \mu s$, $25 \mu s$, and $125 \mu s$ with similar results. Only the data for a $1 \mu s$ annealing time is presented in Figure 5a, see Appendix E for results for the other annealing times.

Because σ_1 and σ_3 are not coupled together in the input Hamiltonian, one expects J_{13} from the reconstruction to be close to zero. However, as shown in Figure 5a, J_{13} appears to be negative and, hence, anti-ferromagnetic below $J_{in} = 0.275$ and positive above that point. In [17], this effect is referred to as a “spurious coupling” because it appears in the output distribution despite not being programmed in the input Hamiltonian. It is striking that this spurious coupling exactly cancels out when $J_{in} = 0.275$, which coincides with the optimal input scaling for α_{in} for which almost all GSD models in Figure 3 are shown to have low total variation. Furthermore, the regime where the spurious coupling strength is low relative to the intended coupling strengths can be expanded

² Note when programming a D-Wave system, negative values of J_{in} are used to follow the ferromagnetic sign convention of that platform.



(a) Reconstructed coupling values for three-spin Ising chain sampled at various coupling strengths. Only J_{12} (coupling between σ_1 and σ_2 represented by green in figure) and J_{23} (coupling between σ_2 and σ_3 represented by red in figure) are programmed in input Hamiltonian. J_{13} (blue) is not included in input Hamiltonian.



(b) Results from model simulation that replicates three-spin Ising chain experiment. J_{12} and J_{23} are identical and only the green line is visible. J_{13} is spurious coupling and represented by blue.

FIG. 5: Notice how J_{13} is reconstructed as negative for low-input couplings and then transitions to positive as input coupling increases beyond 0.275. As this coupling is not programmed in the input Hamiltonian, this non-zero reconstruction marks a disruption to the desired distribution. The negative and positive regions indicate the scaling regimes where noise and quantum effects distort the output distribution, respectively. We observe that the optimal scaling regime to use for Gibbs sampling is when J_{13} is small relative to J_{12} and J_{23} .

to approximately include J_{in} between 0.2 to 0.35, which again closely matches the optimal range for α_{in} that was found for the 16 spin experiments. This provides additional support to the observation that the QA hardware considered here is an effective Gibbs sampler in this specific scaling range.

B. A Three-Qubit Ising Chain Effective Model

To further explore a connection between these experimental observations and the spurious couplings observed in the hardware's output (i.e., Figure 5a), we propose an extension of the effective single-qubit quantum model developed in [17] to the three-qubit context. The single-qubit model considered in [17, 45] includes a transverse field with an intensity proportional to the input local field parameter, h . This transverse field component was able to reproduce an observed saturation of the output field for large input values. Another important feature proposed in [17] was qubit noise perturbing the input parameters of the model, which explained the spurious couplings in the regime of low input parameters. Building on these characteristics, we consider the following toy model on three qubits controlled by a single parameter J_{in} in the absence of local fields. We assume the output distribution is a noise-averaged thermal distribution:

$$\rho = \frac{1}{8} \sum_{s_1, s_2, s_3 = \pm 1} \frac{\exp(-\beta H)}{\text{Tr} \exp(-\beta H)}, \quad (7)$$

where H is a three-qubit Hamiltonian with independent binary qubit noise realized through binary random variables s_i :

$$H = -J_{in}(\hat{\sigma}_1^z \hat{\sigma}_2^z + \hat{\sigma}_2^z \hat{\sigma}_3^z) - \sum_{i=1}^3 \gamma_i J_{in} \hat{\sigma}_i^x - \sum_{i=1}^3 \eta_i s_i \hat{\sigma}_i^z. \quad (8)$$

Equation (8) describes a three-qubit Ising chain, J_{in} is a single input parameter controlling the strength of interactions, while γ_i and η_i are constants re-scaling the strength of the transverse field and qubit noise. Leveraging the parameters estimated in [17], we select $\beta = 11$, $\gamma_i = 0.013$ and $\eta_i = 0.04$ as typical values for these parameters. We would like to highlight that the model from Equation (8) is very different quantitatively and qualitatively from what is known as the Background Susceptibility model as discussed in Appendix F.

It was shown in [17] that for small values of the input parameter J_{in} , the negative spurious coupling can be explained by field noise on the involved qubits. In fact, it is information-theoretically impossible to distinguish between a model with field noise and a model with the corresponding anti-ferromagnetic coupling. As seen in Figure 5b, the toy model in Eq. (7) indeed predicts

that when J_{in} is small and thus field noise is significant relative to J_{in} , a negative spurious coupling is pre-set. We therefore designate this low-scaling regime where $J_{in} < 0.2$ as the noisy regime.

When J_{in} increases, the field noise becomes less pronounced relative to J_{in} . In this regime of higher input values, the model (7) predicts an emergence of a positive spurious coupling – an effect that is also observed in the experimental data. This suggests that a J -dependent residual transverse field on each of the qubits can account for the positive response in spurious link and the saturation of that link for large inputs. Similarly to how we designated the low-scaling regime as noise-dominated, we can designate the high-scaling regime as dominated by the effect of residual transverse fields.

An interesting intermediate regime predicted by the toy model as shown in Figure 5 happens around $J_{in} = 0.275$, where noise and transverse field influences cancel each other, leading to an effective absence of spurious couplings, which also occurs experimentally. This observation suggests that the optimal sampling parameter range for α_{in} , referred to as the *sweet-spot* previously in this work, may be explained by the interacting effects of noise and residual fields in the system.

V. CONCLUSION

Inspired by recent work indicating that quantum annealing hardware behaves as a noisy Gibbs sampler in very low energy scales [17], this work identified a new approach for mitigating the impacts of noise and conducting high-quality Gibbs sampling in a range of effective temperatures for a class of small hardware-native Ising models. This novel approach to using quantum annealing hardware for Gibbs sampling opens new opportunities for applications in machine learning and exploring the physics of condensed matter systems.

More broadly, the computational task of Gibbs sampling and the protocol developed in this work could provide a novel avenue for exploring the potential for quantum advantage in quantum annealing hardware. To that end, two follow-on works would be required. First, a

class of Ising models needs to be identified that are challenging to sample from with classical algorithms (e.g., spin-glasses) that also adhere to the criteria proposed in this work, i.e., naively representable on the hardware with $h, J \in \{-1, 0, 1\}$. Such examples seem unlikely in the Chimera hardware architecture [58, 60]; however, the new Pegasus hardware architecture [61] will likely provide new opportunities for identifying such models. Second, significant additional research is required to verify that the protocol proposed by this work will scale to larger systems, ideally with 100's to 1000's of qubits, so that more of the quantum annealing hardware can be used. This type of verification requires an amazing amount of computation and tuning of sophisticated Monte Carlo methods as there are no known efficient algorithms for generating Gibbs samples of the target distributions that would be required as a baseline of comparison. Another practical challenge is that scaling to larger systems may also yield unexpected side effects in practice, such as amplifying the role of hardware programming errors [62, 63], putting an implicit limit on sampling accuracy at larger scales. Although significant follow-on investigation is required to more deeply understand the potential for performing thermal Gibbs sampling with quantum annealing hardware, this work provides a foundation for maximizing the performance available hardware platforms when conducting these computational tasks.

VI. ACKNOWLEDGEMENTS

This work was supported by the U.S. DOE through the Laboratory Directed Research and Development (LDRD) program of LANL under project number 20210114ER. This research used computing resources provided by the LANL Institutional Computing Program, which is supported by the U.S. Department of Energy National Nuclear Security Administration under Contract No. 89233218CNA000001. This material is also based upon work supported by the National Science Foundation of the Quantum Leap Big Idea under Grant No. OMA-1936388.

-
- [1] Alistair Sinclair and Mark Jerrum, “Approximate counting, uniform generation and rapidly mixing markov chains,” *Information and Computation* **82**, 93–133 (1989).
 - [2] Mark R Jerrum, Leslie G Valiant, and Vijay V Vazirani, “Random generation of combinatorial structures from a uniform distribution,” *Theoretical computer science* **43**, 169–188 (1986).
 - [3] Mark Jerrum and Alistair Sinclair, “Polynomial-time approximation algorithms for the ising model,” *SIAM Journal on computing* **22**, 1087–1116 (1993).
 - [4] Giovanni Gallavotti, *Statistical mechanics: A short treatise* (Springer Science & Business Media, 2013).
 - [5] Joshua Job and Daniel Lidar, “Test-driving 1000 qubits,” *Quantum Science and Technology* **3**, 030501 (2018).
 - [6] Alejandro Perdomo-Ortiz, Marcello Benedetti, John Realpe-Gómez, and Rupak Biswas, “Opportunities and challenges for quantum-assisted machine learning in near-term quantum computers,” *Quantum Science and Technology* **3**, 030502 (2018).
 - [7] Takahiro Inagaki, Yoshitaka Haribara, Koji Igarashi, Tomohiro Sonobe, Shuhei Tamate, Toshimori Honjo, Alireza Marandi, Peter L McMahan, Takeshi Umeki,

- Koji Enbutsu, *et al.*, “A coherent ising machine for 2000-node optimization problems,” *Science* **354**, 603–606 (2016).
- [8] Frank Arute, Kunal Arya, Ryan Babbush, Dave Bacon, Joseph C Bardin, Rami Barends, Rupak Biswas, Sergio Boixo, Fernando GSL Brandao, David A Buell, *et al.*, “Quantum supremacy using a programmable superconducting processor,” *Nature* **574**, 505–510 (2019).
- [9] Tadashi Kadowaki and Hidetoshi Nishimori, “Quantum annealing in the transverse ising model,” *Phys. Rev. E* **58**, 5355–5363 (1998).
- [10] J. Brooke, D. Bitko, T. F. Rosenbaum, and G. Aeppli, “Quantum annealing of a disordered magnet,” *Science* **284**, 779–781 (1999).
- [11] J. Brooke, T. F. Rosenbaum, and G. Aeppli, “Tunable quantum tunnelling of magnetic domain walls,” *Nature* **413**, 610–613 (2001).
- [12] Edward Farhi, Jeffrey Goldstone, Sam Gutmann, Joshua Lapan, Andrew Lundgren, and Daniel Preda, “A quantum adiabatic evolution algorithm applied to random instances of an np-complete problem,” *Science* **292**, 472–475 (2001).
- [13] Zhengbing Bian, Fabian Chudak, William G. Macready, and Geordie Rose, “The ising model: teaching an old problem new tricks,” Published online at https://www.dwavesys.com/sites/default/files/weightedmaxsat_v2.pdf (2010), accessed: 04/28/2017.
- [14] Jack Raymond, Sheir Yarkoni, and Evgeny Andriyash, “Global warming: Temperature estimation in annealers,” *Frontiers in ICT* **3**, 23 (2016).
- [15] Jeffrey Marshall, Eleanor G. Rieffel, and Itay Hen, “Thermalization, freeze-out, and noise: Deciphering experimental quantum annealers,” *Phys. Rev. Applied* **8**, 064025 (2017).
- [16] Jeffrey Marshall, Davide Venturelli, Itay Hen, and Eleanor G. Rieffel, “Power of pausing: Advancing understanding of thermalization in experimental quantum annealers,” *Phys. Rev. Applied* **11**, 044083 (2019).
- [17] Marc Vuffray, Carleton Coffrin, Yaroslav A Kharkov, and Andrey Y Likhov, “Programmable quantum annealers as noisy gibbs samplers,” arXiv preprint arXiv:2012.08827 (2020).
- [18] Marcello Benedetti, John Realpe-Gómez, Rupak Biswas, and Alejandro Perdomo-Ortiz, “Estimation of effective temperatures in quantum annealers for sampling applications: A case study with possible applications in deep learning,” *Phys. Rev. A* **94**, 022308 (2016).
- [19] Marcello Benedetti, John Realpe-Gómez, Rupak Biswas, and Alejandro Perdomo-Ortiz, “Quantum-assisted learning of hardware-embedded probabilistic graphical models,” *Phys. Rev. X* **7**, 041052 (2017).
- [20] John J Hopfield, “Neural networks and physical systems with emergent collective computational abilities,” *Proceedings of the national academy of sciences* **79**, 2554–2558 (1982).
- [21] Dileep Kumar Panjwani and Glenn Healey, “Markov random field models for unsupervised segmentation of textured color images,” *IEEE Transactions on pattern analysis and machine intelligence* **17**, 939–954 (1995).
- [22] Andrey Y. Likhov, Marc Vuffray, Sidhant Misra, and Michael Chertkov, “Optimal structure and parameter learning of Ising models,” *Science Advances* **4** (2018), 10.1126/sciadv.1700791.
- [23] Gary Kochenberger, Jin-Kao Hao, Fred Glover, Mark Lewis, Zhipeng Lü, Haibo Wang, and Yang Wang, “The unconstrained binary quadratic programming problem: a survey,” *Journal of Combinatorial Optimization* **28**, 58–81 (2014).
- [24] A. Einstein, “Beiträge z. quantentheorie,” *Verh. d. D. phys. Ges.* **16**, 826 (1914).
- [25] M. Born and V. Fock, “Beweis des adiabatsatzes,” *Zeit. f. Physik* **51**, 165–196 (1928).
- [26] P. Ehrenfest, “Over adiabatische veranderingen van een stelsel in verband met de theorie der quanta,” *Verslagen Kon. Akad. Amserdam* **25**, 412 – 433 (1916).
- [27] T. Kato, “On the adiabatic theorem of quantum mechanics,” *J. Phys. Soc. Jap.* **5**, 435 (1950).
- [28] Sabine Jansen, Mary-Beth Ruskai, and Ruedi Seiler, “Bounds for the adiabatic approximation with applications to quantum computation,” *J. Math. Phys.* **48**, 102111 (2007).
- [29] Yoshiki Matsuda, Hidetoshi Nishimori, and Helmut G Katzgraber, “Quantum annealing for problems with ground-state degeneracy,” *Journal of Physics: Conference Series* **143**, 012003 (2009).
- [30] Sergio Boixo, Tameem Albash, Federico M. Spedalieri, Nicholas Chancellor, and Daniel A. Lidar, “Experimental signature of programmable quantum annealing,” *Nature Communications* **4**, 2067 (2013).
- [31] Brian Hu Zhang, Gene Wagenbreth, Victor Martin-Mayor, and Itay Hen, “Advantages of unfair quantum ground-state sampling,” *Scientific Reports* **7**, 1044 (2017).
- [32] Mario S. Könz, Guglielmo Mazzola, Andrew J. Ochoa, Helmut G. Katzgraber, and Matthias Troyer, “Uncertain fate of fair sampling in quantum annealing,” *Phys. Rev. A* **100**, 030303 (2019).
- [33] Vaibhaw Kumar, Casey Tomlin, Curt Nehr Korn, Daniel O’Malley, and Joseph Dulny III, “Achieving fair sampling in quantum annealing,” (2020), arXiv:2007.08487.
- [34] Elijah Pelofske, John Golden, Andreas Bärtzchi, Daniel O’Malley, and Stephan Eidenbenz, “Sampling on nisq devices: ”who’s the fairest one of all?,” (2021), arXiv:2107.06468.
- [35] Tameem Albash and Daniel A. Lidar, “Decoherence in adiabatic quantum computation,” *Phys. Rev. A* **91**, 062320 (2015).
- [36] Sergio Boixo, Vadim N. Smelyanskiy, Alireza Shabani, Sergei V. Isakov, Mark Dykman, Vasil S. Denchev, Mohammad H. Amin, Anatoly Yu Smirnov, Masoud Mohseni, and Hartmut Neven, “Computational multi-qubit tunnelling in programmable quantum annealers,” *Nature Communications* **7**, 10327 (2016).
- [37] Anatoly Yu Smirnov and Mohammad H Amin, “Theory of open quantum dynamics with hybrid noise,” *New Journal of Physics* **20**, 103037 (2018).
- [38] Walid K. Abou Salem, “On the quasi-static evolution of nonequilibrium steady states,” *Annales Henri Poincaré* **8**, 569–596 (2007).
- [39] J. E. Avron, M. Fraas, G. M. Graf, and P. Grech, “Adiabatic theorems for generators of contracting evolutions,” *Communications in Mathematical Physics* **314**, 163–191 (2012).
- [40] Lorenzo Campos Venuti, Tameem Albash, Daniel A. Lidar, and Paolo Zanardi, “Adiabaticity in open quantum systems,” *Phys. Rev. A* **93**, 032118 (2016), 1508.05558.

- [41] G. Lindblad, “On the generators of quantum dynamical semigroups,” *Communications in Mathematical Physics* **48**, 119–130 (1976).
- [42] E. B. Davies, “Markovian master equations,” *Communications in Mathematical Physics* **39**, 91–110 (1974).
- [43] Tameem Albash, Sergio Boixo, Daniel A Lidar, and Paolo Zanardi, “Quantum adiabatic markovian master equations,” *New Journal of Physics* **14**, 123016 (2012), 1206.4197.
- [44] D-Wave Systems Inc., “D-wave system documentation,” Published online at <https://docs.dwavesys.com/docs/latest/> (2020), accessed: 03/17/2021.
- [45] Jon Nelson, Marc Vuffray, Andrey Y. Lokhov, and Carleton Coffrin, “Single-qubit fidelity assessment of quantum annealing hardware,” *IEEE Transactions on Quantum Engineering*, 1–1 (2021).
- [46] Mohammad H. Amin, “Searching for quantum speedup in quasistatic quantum annealers,” *Phys. Rev. A* **92**, 052323 (2015).
- [47] Mohammad H. Amin, Evgeny Andriyash, Jason Rolfe, Bohdan Kulchitsky, and Roger Melko, “Quantum boltzmann machine,” *Phys. Rev. X* **8**, 021050 (2018).
- [48] Walter Vinci, Lorenzo Buffoni, Hossein Sadeghi, Amir Khoshaman, Evgeny Andriyash, and Mohammad H Amin, “A path towards quantum advantage in training deep generative models with quantum annealers,” *Machine Learning: Science and Technology* **1**, 045028 (2020).
- [49] R. Harris, Y. Sato, A. J. Berkley, M. Reis, F. Altomare, M. H. Amin, K. Boothby, P. Bunyk, C. Deng, C. Enderud, S. Huang, E. Hoskinson, M. W. Johnson, E. Ladizinsky, N. Ladizinsky, T. Lanting, R. Li, T. Medina, R. Molavi, R. Neufeld, T. Oh, I. Pavlov, I. Perminov, G. Poulin-Lamarre, C. Rich, A. Smirnov, L. Swenson, N. Tsai, M. Volkmann, J. Whittaker, and J. Yao, “Phase transitions in a programmable quantum spin glass simulator,” *Science* **361**, 162–165 (2018).
- [50] Andrew D. King, Juan Carrasquilla, Jack Raymond, Isil Ozfidan, Evgeny Andriyash, Andrew Berkley, Mauricio Reis, Trevor Lanting, Richard Harris, Fabio Altomare, Kelly Boothby, Paul I. Bunyk, Colin Enderud, Alexandre Fréchet, Emile Hoskinson, Nicolas Ladizinsky, Travis Oh, Gabriel Poulin-Lamarre, Christopher Rich, Yuki Sato, Anatoly Yu. Smirnov, Loren J. Swenson, Mark H. Volkmann, Jed Whittaker, Jason Yao, Eric Ladizinsky, Mark W. Johnson, Jeremy Hilton, and Mohammad H. Amin, “Observation of topological phenomena in a programmable lattice of 1,800 qubits,” *Nature* **560**, 456–460 (2018).
- [51] Andrew D. King, Cristiano Nisoli, Edward D. Dahl, Gabriel Poulin-Lamarre, and Alejandro Lopez-Bezanilla, “Qubit spin ice,” *Science* (2021), 10.1126/science.abe2824.
- [52] Jeffrey Marshall, Andrea Di Gioacchino, and Eleanor G. Rieffel, “Perils of embedding for sampling problems,” *Phys. Rev. Research* **2**, 023020 (2020).
- [53] Richard Y Li, Tameem Albash, and Daniel A Lidar, “Limitations of error corrected quantum annealing in improving the performance of boltzmann machines,” *Quantum Science and Technology* **5**, 045010 (2020).
- [54] Tristan Zaborniak and Rogério de Sousa, “Benchmarking hamiltonian noise in the d-wave quantum annealer,” *IEEE Transactions on Quantum Engineering* **2**, 1–6 (2021).
- [55] P. I. Bunyk, E. M. Hoskinson, M. W. Johnson, E. Tolkaheva, F. Altomare, A. J. Berkley, R. Harris, J. P. Hilton, T. Lanting, A. J. Przybysz, and J. Whittaker, “Architectural considerations in the design of a superconducting quantum annealing processor,” *IEEE Transactions on Applied Superconductivity* **24**, 1–10 (2014).
- [56] Troels F. Rønnow, Zhihui Wang, Joshua Job, Sergio Boixo, Sergei V. Isakov, David Wecker, John M. Martinis, Daniel A. Lidar, and Matthias Troyer, “Defining and detecting quantum speedup,” *Science* **345**, 420–424 (2014).
- [57] Tameem Albash, Walter Vinci, Anurag Mishra, Paul A. Warburton, and Daniel A. Lidar, “Consistency tests of classical and quantum models for a quantum annealer,” *Phys. Rev. A* **91**, 042314 (2015).
- [58] Helmut G. Katzgraber, Firas Hamze, and Ruben S. Andrist, “Glassy chimeras could be blind to quantum speedup: Designing better benchmarks for quantum annealing machines,” *Phys. Rev. X* **4**, 021008 (2014).
- [59] Marc Vuffray, Sidhant Misra, Andrey Lokhov, and Michael Chertkov, “Interaction screening: Efficient and sample-optimal learning of Ising models,” in *Advances in Neural Information Processing Systems*, Vol. 29, edited by D. Lee, M. Sugiyama, U. Luxburg, I. Guyon, and R. Garnett (Curran Associates, Inc., 2016).
- [60] Martin Weigel, Helmut G. Katzgraber, Jonathan Machta, Firas Hamze, and Ruben S. Andrist (Octomore Collaboration), “Erratum: Glassy chimeras could be blind to quantum speedup: Designing better benchmarks for quantum annealing machines [phys. rev. x 4, 021008 (2014)],” *Phys. Rev. X* **5**, 019901 (2015).
- [61] Kelly Boothby, Paul Bunyk, Jack Raymond, and Aidan Roy, “Next-Generation Topology of D-Wave Quantum Processors,” *arXiv e-prints*, arXiv:2003.00133 (2020), arXiv:2003.00133 [quant-ph].
- [62] Zheng Zhu, Andrew J. Ochoa, Stefan Schnabel, Firas Hamze, and Helmut G. Katzgraber, “Best-case performance of quantum annealers on native spin-glass benchmarks: How chaos can affect success probabilities,” *Phys. Rev. A* **93**, 012317 (2016).
- [63] Tameem Albash, Victor Martin-Mayor, and Itay Hen, “Analog errors in ising machines,” *Quantum Science and Technology* **4**, 02LT03 (2019).
- [64] Sergio Boixo, Troels F. Rønnow, Sergei V. Isakov, Zhihui Wang, David Wecker, Daniel A. Lidar, John M. Martinis, and Matthias Troyer, “Evidence for quantum annealing with more than one hundred qubits,” *Nature Physics* **10**, 218–224 (2014).
- [65] Carleton Coffrin, Harsha Nagarajan, and Russell Bent, “Evaluating ising processing units with integer programming,” in *Integration of Constraint Programming, Artificial Intelligence, and Operations Research*, edited by Louis-Martin Rousseau and Kostas Stergiou (Springer International Publishing, Cham, 2019) pp. 163–181.

Appendix A: Comparing Distributions with Total Variation Distance

Given two distributions μ and ν over a binary string of size N , i.e. $\sigma \in \{-1, 1\}^N$, the total variation between them is defined as,

$$\text{TV}(\mu, \nu) = \frac{1}{2} \sum_{\sigma \in \{-1, 1\}^N} |\mu(\sigma) - \nu(\sigma)|, \quad (\text{A1})$$

that is, the absolute difference between the probability of each state divided by 2, to normalize the metric to the range of 0 to 1. Given that the metric is in the range of 0 to 1, it is often presented as a percentage between 0 and 100.

The TV distance can be interpreted as the maximum discrepancy between the probability of an event computed with the distribution μ instead of ν , that is,

$$\sup_A |\mathbb{P}_\mu(A) - \mathbb{P}_\nu(A)| = \text{TV}(\mu, \nu), \quad (\text{A2})$$

where $A \in \mathcal{P}(\{-1, 1\}^N)$ is an element of the power set of $\{-1, 1\}^N$. Therefore, it comes as the distance of choice to measure the error that can be made by estimating probabilities using a surrogate distribution ν of a target distribution μ . However, note that this sets a very strong quality criteria for estimating the reliability of a surrogate distribution as the TV is equal to the worst-case estimation error. It is important to note that if μ or ν are only accessible through a set of finite samples, there is an unavoidable error caused by sampling that will be captured by the TV distance. To avoid finite sampling error in the TV estimate, one needs to use a number of samples that is on the order of the typical support of μ and ν . This is required to estimate the absolute difference in Eq. (A1) accurately for each state σ . Typically, the number of samples required grows exponentially in N and is maximal for distribution μ and ν that are close to a uniform distribution where it is in the order of 2^N .

It is fairly common to consider KL divergence as an alternative to the TV distance, especially when the non-convexity of the latter becomes a computational bottleneck, taking advantage of Pinsker's inequality, i.e., $\text{TV}(\mu, \nu) \leq \sqrt{1/2 \text{KL}(\mu||\nu)}$. However, the KL divergence does not share the same meaning as the TV distance: the KL divergence estimates the inefficiency in compressing a source μ using a code optimized for ν . In general, it is not suitable for measuring the quality of probability estimates between a target distribution and its surrogate. A simple situation that illustrates this last point is when the distribution ν is almost identical to μ except that it has an infinitesimally small probability mass that lies outside of the support of μ . The TV distance between these distribution is infinitesimally small, while the KL divergence becomes infinite.

Appendix B: The Ground State Degeneracy Models

The Ising model instances used in this work were generated by the following procedure. First, 16 spins (2 unit cells) on the D-Wave 2000Q Quantum Annealer DW_2000Q_LANL hardware graph were selected with qubits 296 to 303 making up one unit cell and qubits 304 to 311 making up an adjacent unit cell in the Chimera graph architecture. Then the values for J_{ij} incident to these qubits were assigned randomly from the set $\{-1, 1\}$ for each coupler in the hardware graph. Second, a brute-force calculation was used to compute the ground-state degeneracy for a given instance.³ This procedure was repeated many times and a subset of cases were selected to highlight a smooth range of ground-state degeneracies. This yielded a total of seven GSD (ground-state degeneracy) cases with degeneracy values of 2, 4, 6, 8, 10, 24, and 38, which are presented in Table II. The same procedure was repeated while also assigning random values to the local fields h_i to $\{-1, 1\}$, yielding six additional GSD-F models with 1, 2, 3, 4, 5, and 6 ground state degeneracies, which are presented in Table III. The specific instances are referred to as GSD-# and GSD-F-#, where the # indicates the amount of ground state degeneracy. Note that the GSD-F models tend to have lower degeneracy because the inclusion of the fields breaks symmetries within energy levels.

It is worth noting that these models are reminiscent of the RAN and RANF models that have been used to benchmark earlier generations of QA processors [64, 65]. The RAN model class on Chimera graphs has been shown to exhibit a zero temperature phase transition [58, 60], indicating that sampling from this model class at finite temperature is not expected to be computationally hard. Here however instances are hand-picked from this class to exhibit varying degrees of ground state degeneracy breaking by the transverse field. In this sense, we do not expect that the instances of this work to be representative samples from the RAN class, and instead expect them to be challenging for a quantum annealer to sample from.

Appendix C: Total Variation at Different Scales and Annealing Times

In this section, we present supplementary figures for each of the experiments in the main text. Figures 7 and 8 display the total variation results for every GSD model as a function of α_{in} . As in Figure 1 where only GSD-6 is shown, the results for each of the annealing times are overlaid with different colors. Note how GSD-2 and GSD-F-1 are the only instances where total variation decreases as α_{in} increases. This is because models with low degeneracy are easier to sample from in the high scale regime,

³ This approach is only computationally feasible for small systems spins, such the ones considered here.

which was previously explained in Section III B 2. For the rest of the instances, the consistent U-shaped trend supports our claim that the most effective α_{in} for achieving high accuracy is in the medium scale regime. This optimal band between α_{in} of 0.2 and 0.4 remains consistent across all GSD models. In addition, these figures show that varying annealing time does not shift the optimal region by a significant amount, with the exception of GSD-10. However, there is a slight yet noticeable shift to the left in almost all instances as anneal times increase.

Figure 9 communicates the same information as Figures 7 and 8, but more directly compares various GSD models by stacking their total variation values in a heatmap. Only the $1\mu s$ plot was presented in Figure 3 in the main text, but here the results for all anneal times are shown. Once again, it is evident that the optimal region for α_{in} remains the same for various anneal times.

Appendix D: Effective Temperatures at Different Scales and Annealing Times

Figures 9 and 10 present the α_{out} values that correspond to the optimal α_{in} range between 0.2 and 0.4. The minimum and maximum value in each heatmap was used to construct Table I. These figures show how α_{in} and anneal time can be used to smoothly tune α_{out} and that the effect is consistent across all GSD models. Although the exact α_{out} values vary slightly from model to model, the trend is predictable and so these figures suggest a straightforward approach for producing Gibbs samples at at desired α_{out} value.

Appendix E: Three-Spin Ising Chain Annealing Times

Finally, Figure 13 shows results for the three-spin Ising chain experiment for various anneal times. The most important feature of these plots is the point at which the spurious coupling reduces to zero, as we hypothesize that this is the optimal input scale for sampling. From the plots, this optimal J_{in} value slightly decreases from 0.275 to a low of 0.2 as anneal time increases. However, this value still remains within the optimal region seen in the 16-spin scaling experiments. As anneal time increases, both programmed and spurious couplings appear to increase more rapidly with the increase of J_{in} . This increase results in the spurious coupling almost saturating by the time J_{in} reaches 0.4 for anneal times of $25\ \mu s$ and $125\ \mu s$. However, the majority of our claimed optimal region between 0.2 and 0.4 remains in the regime where the spurious

coupling is small compared to the programmed couplings.

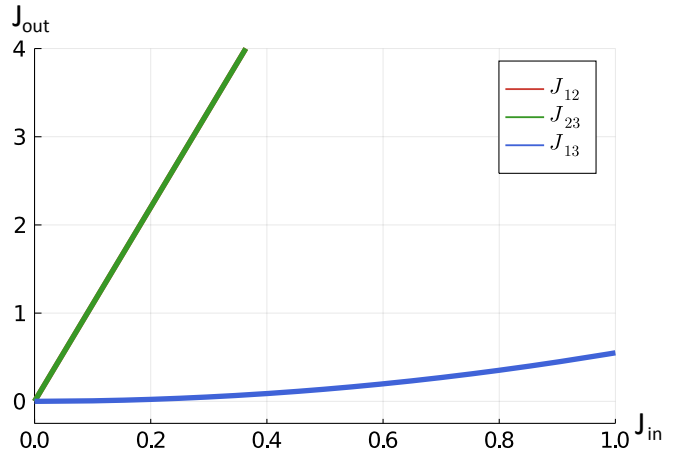


FIG. 6: Input and spurious coupling values as a function of the input coupling intensity according to the Background susceptibility model.

Appendix F: Background Susceptibility Model for the Three-Spin Ising Chain

It is believed that physically neighboring qubits are not perfectly isolated from each other and give rise to uncontrolled interactions. These spurious couplings are described by the Background Susceptibility model [44] and take the form of an interaction that is proportional to the coupling intensities emanating from neighboring qubits. For the three-spin Ising chain discussed in Section IV, it results in the following Hamiltonian with background susceptibility,

$$H_{BS} = -J_{in}\hat{\sigma}_1^z\hat{\sigma}_2^z - J_{in}\hat{\sigma}_2^z\hat{\sigma}_3^z - \chi J_{in}^2\hat{\sigma}_1^z\hat{\sigma}_3^z, \quad (F1)$$

where $\chi > 0$ is the background susceptibility constant⁴ between qubits one and three. Notice that the intensity of the spurious link between σ_1 and σ_3 is quadratic in the input coupling intensity J_{in} and is of ferromagnetic nature when J_{in} is positive. Because the Hamiltonian in Eq. (F1) is diagonal, we immediately see that this model behaves very differently than the effective Hamiltonian found experimentally (see Figure 5). The background susceptibility model predicts no saturation in the input coupling or spurious coupling intensity, as the earlier grow linearly and the later grows quadratically. Moreover, the spurious coupling of the background susceptibility model remains ferromagnetic unlike what is measured experimentally for small values of J_{in} . This behavior is depicted in Figure F1 for the typically encountered values of $\beta = 11$ and $\chi = 0.05$.

⁴ In [44], χ is a negative quantity following the D-Wave programming convention that ferromagnetic couplings are negative.

	GSD-2	GSD-4	GSD-6	GSD-8	GSD-10	GSD-24	GSD-38
$J_{296,300}$	1.0	-1.0	1.0	1.0	-1.0	1.0	1.0
$J_{296,301}$	1.0	1.0	-1.0	-1.0	1.0	1.0	1.0
$J_{296,302}$	-1.0	1.0	-1.0	-1.0	-1.0	-1.0	-1.0
$J_{296,303}$	-1.0	-1.0	1.0	-1.0	1.0	-1.0	1.0
$J_{297,300}$	1.0	1.0	1.0	-1.0	-1.0	-1.0	1.0
$J_{297,301}$	1.0	1.0	1.0	1.0	-1.0	1.0	1.0
$J_{297,302}$	-1.0	-1.0	1.0	-1.0	1.0	-1.0	1.0
$J_{297,303}$	1.0	-1.0	-1.0	1.0	-1.0	-1.0	-1.0
$J_{298,300}$	-1.0	1.0	-1.0	1.0	-1.0	-1.0	-1.0
$J_{298,301}$	1.0	-1.0	-1.0	-1.0	-1.0	1.0	1.0
$J_{298,302}$	1.0	1.0	-1.0	1.0	1.0	-1.0	-1.0
$J_{298,303}$	1.0	1.0	1.0	-1.0	-1.0	1.0	-1.0
$J_{299,300}$	1.0	1.0	1.0	-1.0	-1.0	1.0	-1.0
$J_{299,301}$	1.0	-1.0	-1.0	-1.0	1.0	1.0	-1.0
$J_{299,302}$	-1.0	1.0	-1.0	-1.0	1.0	-1.0	1.0
$J_{299,303}$	-1.0	1.0	1.0	-1.0	1.0	-1.0	-1.0
$J_{300,308}$	1.0	-1.0	-1.0	-1.0	-1.0	1.0	1.0
$J_{301,309}$	1.0	1.0	-1.0	-1.0	-1.0	1.0	1.0
$J_{302,310}$	1.0	1.0	1.0	1.0	1.0	-1.0	-1.0
$J_{303,311}$	-1.0	1.0	1.0	-1.0	-1.0	-1.0	1.0
$J_{304,308}$	1.0	-1.0	1.0	-1.0	1.0	1.0	1.0
$J_{304,309}$	1.0	-1.0	1.0	-1.0	-1.0	-1.0	-1.0
$J_{304,310}$	1.0	1.0	-1.0	1.0	-1.0	1.0	-1.0
$J_{304,311}$	-1.0	1.0	1.0	-1.0	-1.0	1.0	1.0
$J_{305,308}$	-1.0	1.0	1.0	1.0	-1.0	-1.0	-1.0
$J_{305,309}$	-1.0	-1.0	1.0	1.0	-1.0	-1.0	-1.0
$J_{305,310}$	-1.0	1.0	-1.0	-1.0	1.0	1.0	-1.0
$J_{305,311}$	-1.0	-1.0	1.0	1.0	1.0	-1.0	-1.0
$J_{306,308}$	1.0	1.0	-1.0	-1.0	-1.0	-1.0	1.0
$J_{306,309}$	-1.0	-1.0	1.0	1.0	-1.0	1.0	1.0
$J_{306,310}$	1.0	1.0	-1.0	1.0	-1.0	-1.0	1.0
$J_{306,311}$	1.0	1.0	1.0	1.0	1.0	1.0	1.0
$J_{307,308}$	1.0	1.0	-1.0	-1.0	-1.0	-1.0	1.0
$J_{307,309}$	1.0	1.0	1.0	1.0	-1.0	1.0	-1.0
$J_{307,310}$	-1.0	-1.0	-1.0	1.0	-1.0	1.0	-1.0
$J_{307,311}$	1.0	-1.0	-1.0	-1.0	1.0	-1.0	1.0

TABLE II: Input coupling values for GSD models before scaling by α_{in} . The D-Wave programming convention is used where negative couplings indicate ferromagnetic and positive couplings indicate antiferromagnetic.

	GSD-F-1	GSD-F-2	GSD-F-3	GSD-F-4	GSD-F-5	GSD-F-6
h_{296}	1.0	1.0	1.0	-1.0	1.0	-1.0
h_{297}	1.0	-1.0	1.0	1.0	-1.0	-1.0
h_{298}	1.0	1.0	-1.0	1.0	-1.0	1.0
h_{299}	1.0	-1.0	-1.0	1.0	-1.0	1.0
h_{300}	-1.0	-1.0	-1.0	-1.0	-1.0	1.0
h_{301}	-1.0	1.0	-1.0	1.0	1.0	1.0
h_{302}	1.0	1.0	1.0	1.0	-1.0	1.0
h_{303}	-1.0	1.0	1.0	-1.0	1.0	-1.0
h_{304}	-1.0	-1.0	1.0	-1.0	-1.0	1.0
h_{305}	-1.0	1.0	-1.0	1.0	1.0	1.0
h_{306}	1.0	-1.0	-1.0	-1.0	-1.0	1.0
h_{307}	1.0	1.0	-1.0	1.0	1.0	-1.0
h_{308}	-1.0	1.0	-1.0	-1.0	1.0	1.0
h_{309}	1.0	-1.0	1.0	-1.0	1.0	1.0
h_{310}	-1.0	1.0	-1.0	-1.0	-1.0	-1.0
h_{311}	-1.0	-1.0	1.0	-1.0	-1.0	-1.0
$J_{296,301}$	-1.0	1.0	1.0	-1.0	-1.0	1.0
$J_{296,302}$	1.0	-1.0	-1.0	1.0	1.0	1.0
$J_{296,303}$	-1.0	-1.0	-1.0	1.0	-1.0	-1.0
$J_{297,300}$	1.0	1.0	1.0	-1.0	1.0	-1.0
$J_{297,301}$	-1.0	-1.0	-1.0	1.0	-1.0	1.0
$J_{297,302}$	1.0	1.0	1.0	1.0	1.0	-1.0
$J_{297,303}$	-1.0	1.0	-1.0	-1.0	1.0	-1.0
$J_{298,300}$	1.0	1.0	1.0	-1.0	-1.0	-1.0
$J_{298,301}$	-1.0	1.0	-1.0	-1.0	-1.0	1.0
$J_{298,302}$	-1.0	-1.0	-1.0	1.0	-1.0	-1.0
$J_{298,303}$	-1.0	-1.0	1.0	-1.0	-1.0	-1.0
$J_{299,300}$	-1.0	1.0	1.0	1.0	1.0	-1.0
$J_{299,301}$	-1.0	1.0	-1.0	-1.0	1.0	1.0
$J_{299,302}$	1.0	-1.0	-1.0	-1.0	-1.0	1.0
$J_{299,303}$	1.0	1.0	1.0	1.0	1.0	1.0
$J_{300,308}$	-1.0	-1.0	1.0	-1.0	1.0	1.0
$J_{301,309}$	-1.0	-1.0	-1.0	-1.0	1.0	1.0
$J_{302,310}$	1.0	1.0	1.0	1.0	-1.0	-1.0
$J_{303,311}$	-1.0	-1.0	-1.0	-1.0	-1.0	1.0
$J_{304,308}$	-1.0	1.0	1.0	1.0	-1.0	-1.0
$J_{304,309}$	-1.0	1.0	1.0	1.0	1.0	-1.0
$J_{304,310}$	1.0	1.0	1.0	-1.0	-1.0	1.0
$J_{304,311}$	1.0	1.0	1.0	-1.0	-1.0	1.0
$J_{305,308}$	-1.0	-1.0	1.0	-1.0	1.0	-1.0
$J_{305,309}$	1.0	-1.0	-1.0	1.0	-1.0	-1.0
$J_{305,310}$	-1.0	-1.0	-1.0	-1.0	1.0	1.0
$J_{305,311}$	1.0	-1.0	1.0	1.0	-1.0	-1.0
$J_{306,308}$	-1.0	1.0	1.0	-1.0	1.0	-1.0
$J_{306,309}$	1.0	1.0	-1.0	-1.0	-1.0	1.0
$J_{306,310}$	1.0	1.0	1.0	1.0	1.0	-1.0
$J_{306,311}$	1.0	-1.0	-1.0	1.0	1.0	1.0
$J_{307,308}$	1.0	1.0	1.0	-1.0	-1.0	1.0
$J_{307,309}$	-1.0	-1.0	-1.0	-1.0	-1.0	1.0
$J_{307,310}$	-1.0	1.0	1.0	-1.0	1.0	1.0
$J_{307,311}$	-1.0	-1.0	-1.0	-1.0	1.0	-1.0

TABLE III: Input coupling and field values for GSD-F models before scaling by α_{in} . The D-Wave programming convention is used where negative couplings indicate ferromagnetic and positive couplings indicate antiferromagnetic.

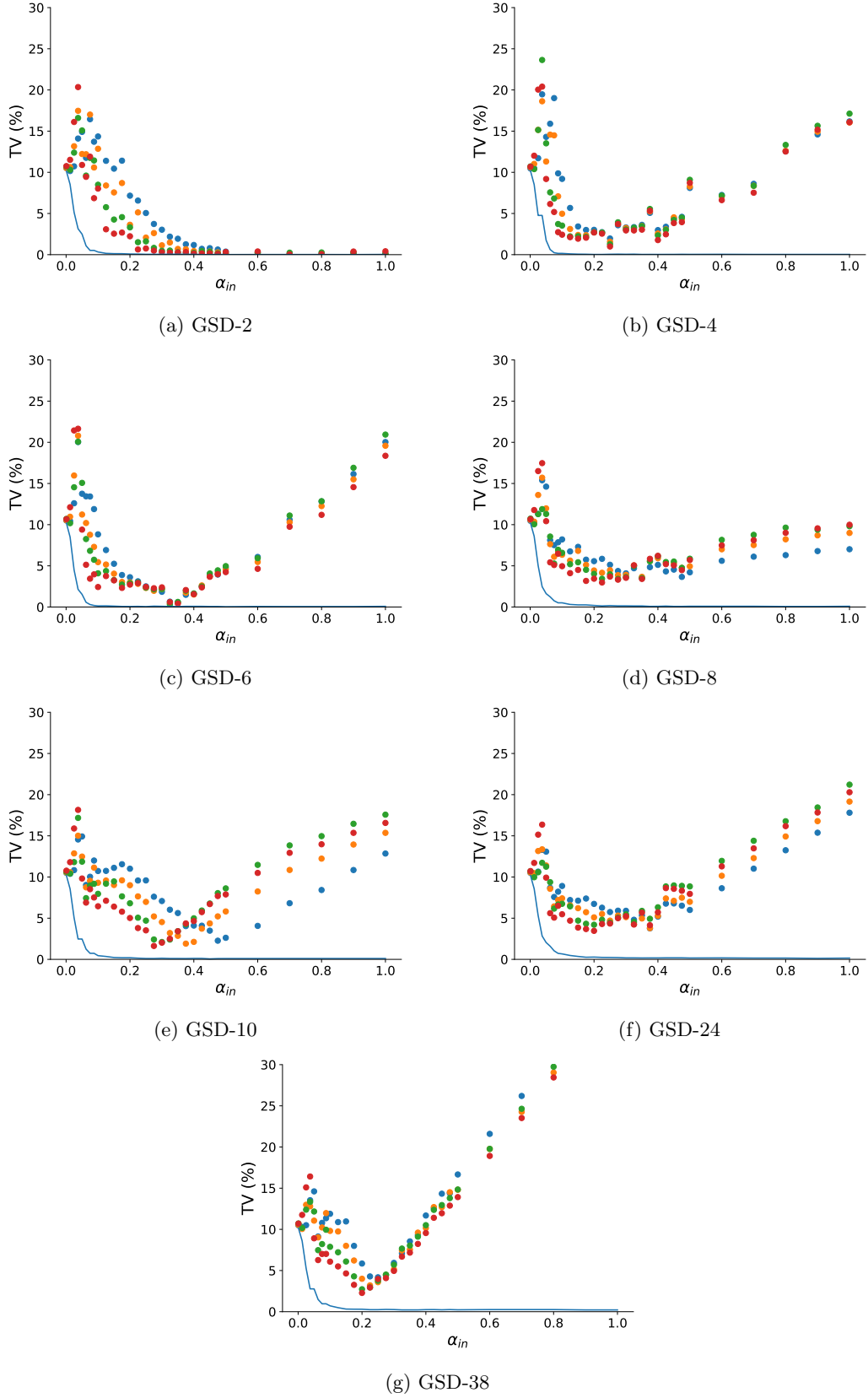
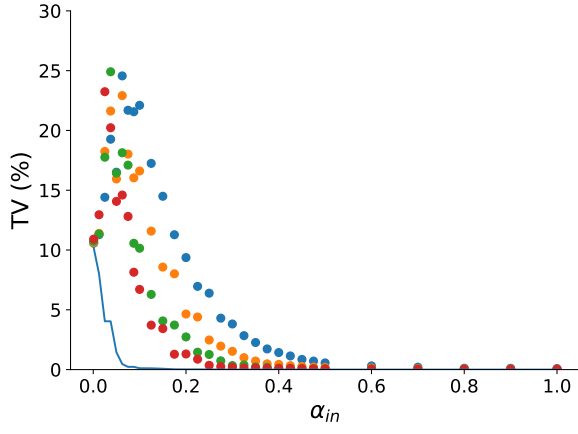
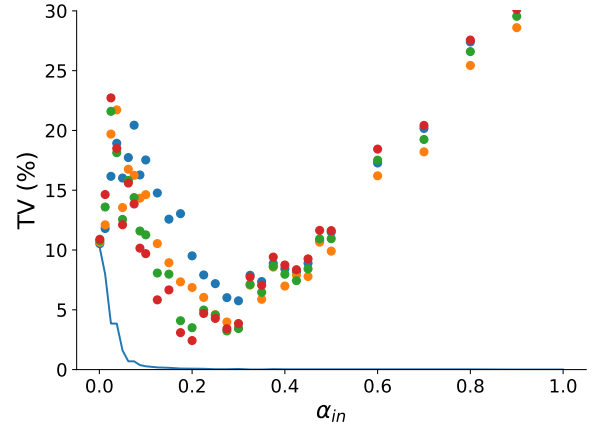


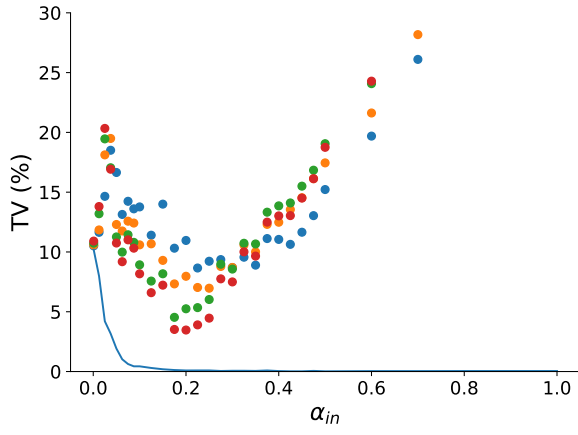
FIG. 7: Dependence of Total Variation on α_{in} for GSD models. Recall from Figure 1 the color notation for various anneal times (blue: $1 \mu s$, orange: $5 \mu s$, green: $25 \mu s$, and red: $125 \mu s$). The TV lower bound is a result of finite sampling is indicated by the blue line.



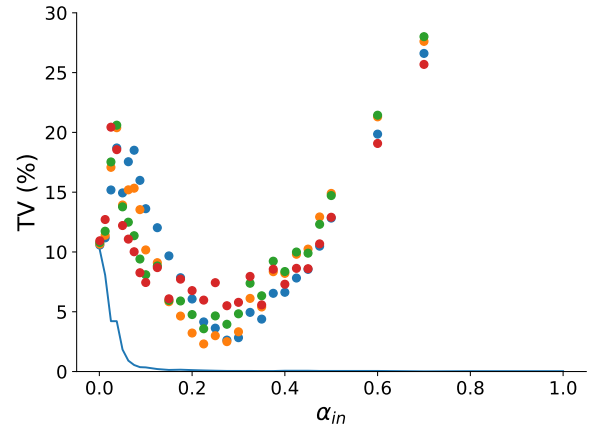
(a) GSD-F-1



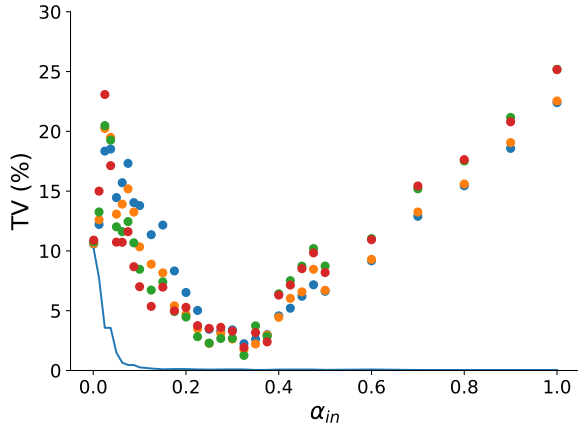
(b) GSD-F-2



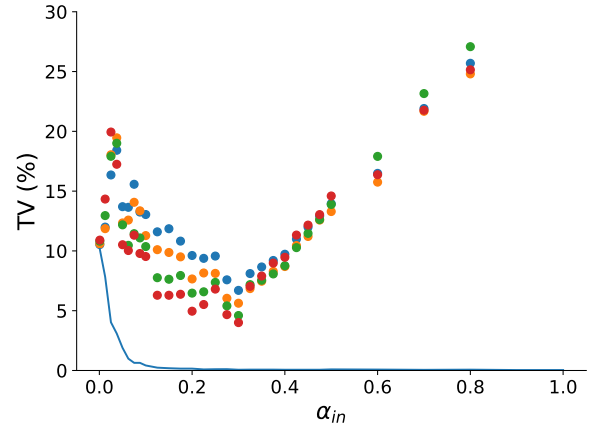
(c) GSD-F-3



(d) GSD-F-4



(e) GSD-F-5



(f) GSD-F-6

FIG. 8: Dependence of Total Variation on α_{in} for GSD-F models. Recall from Figure 1 and 7 the color notation for various anneal times (blue: $1 \mu s$, orange: $5 \mu s$, green: $25 \mu s$, and red: $125 \mu s$). The TV lower bound resulting from finite sampling is indicated by the blue line.

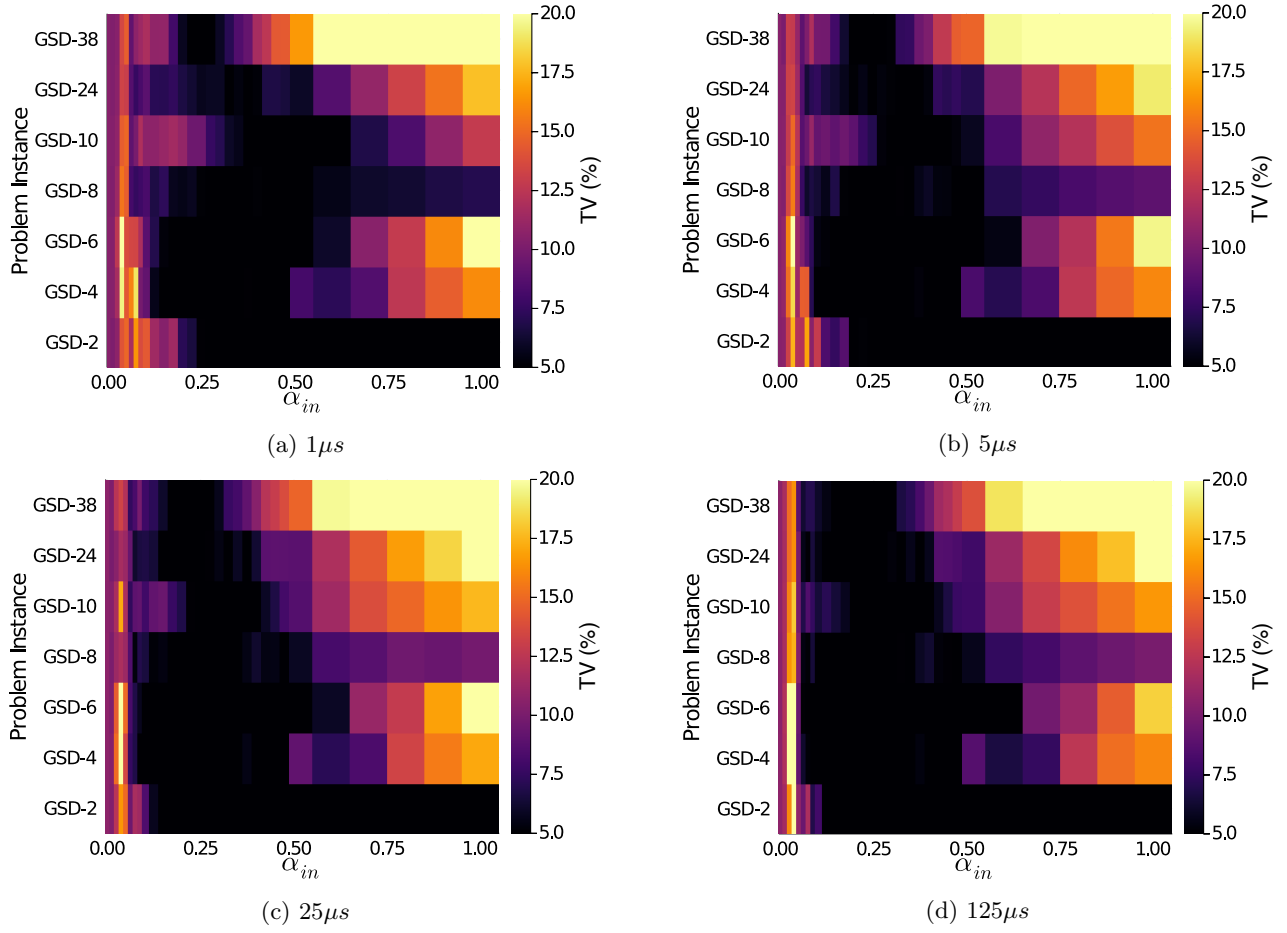


FIG. 9: A heatmap summary of the dependence of total variation on α_{in} and annealing time for all GSD models.

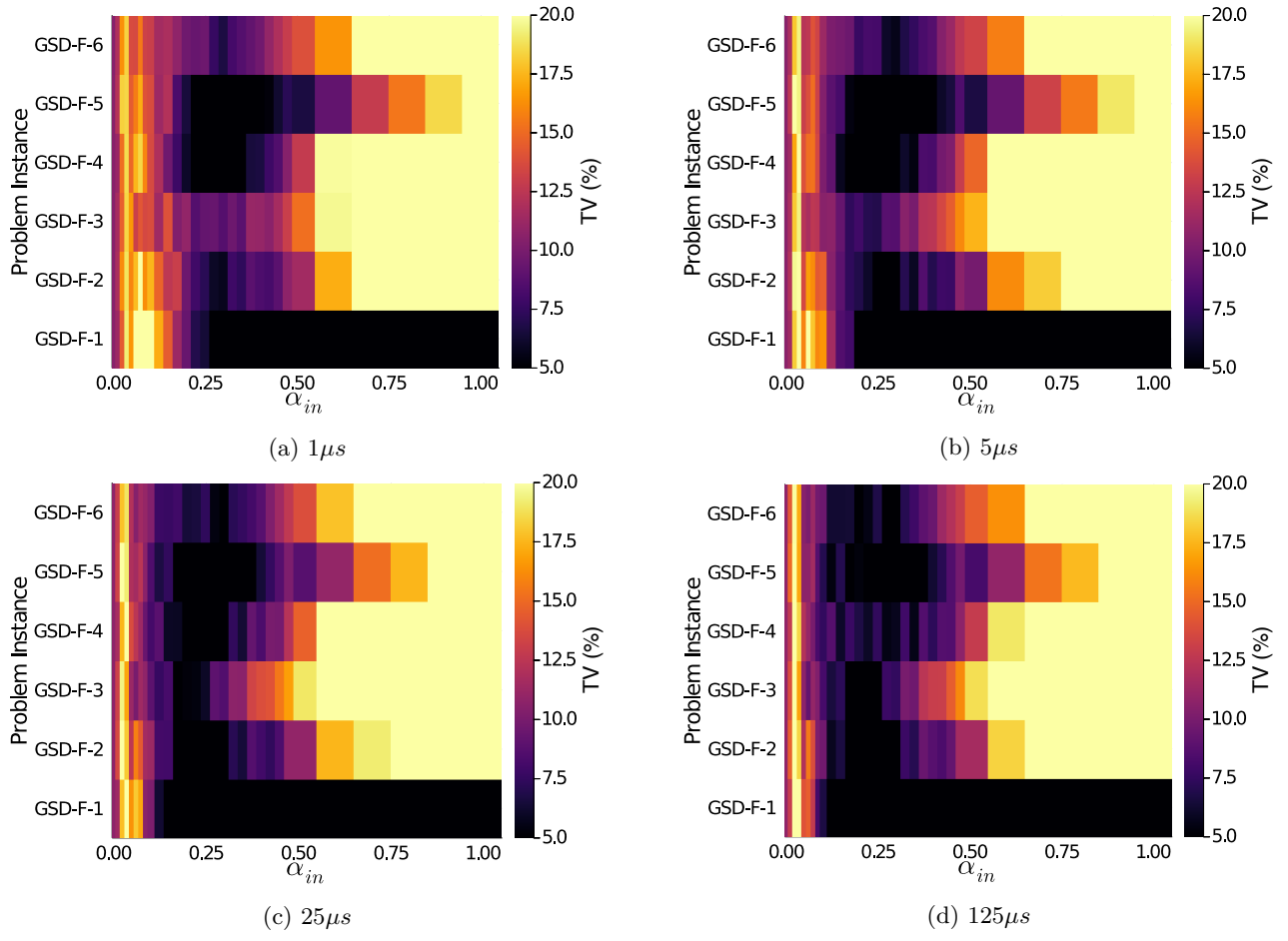


FIG. 10: A heatmap summary of the dependence of total variation on α_{in} and annealing time for all GSD-F models.

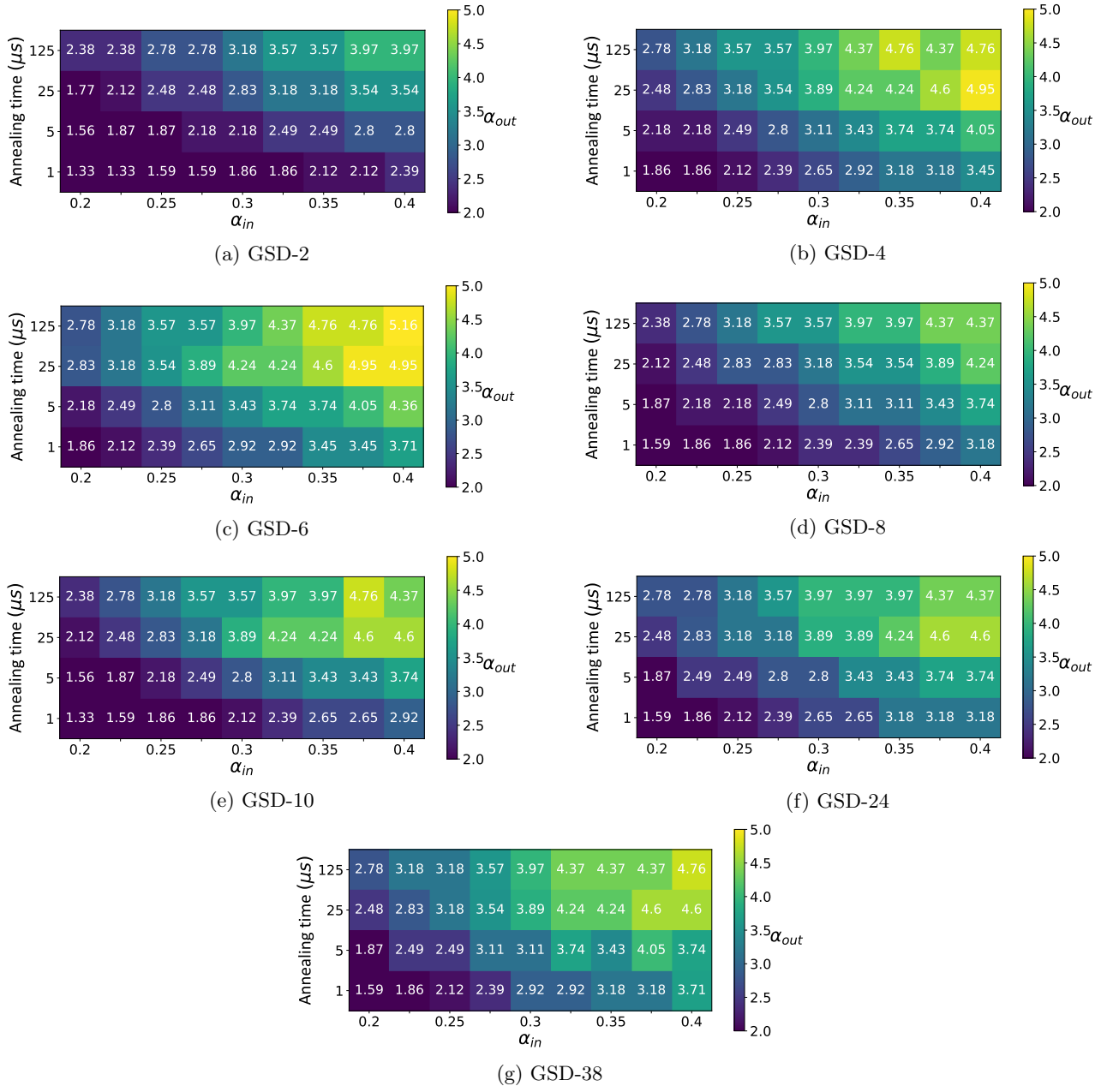


FIG. 11: The dependence of effective temperature α_{out} on α_{in} and annealing time for all GSD models.

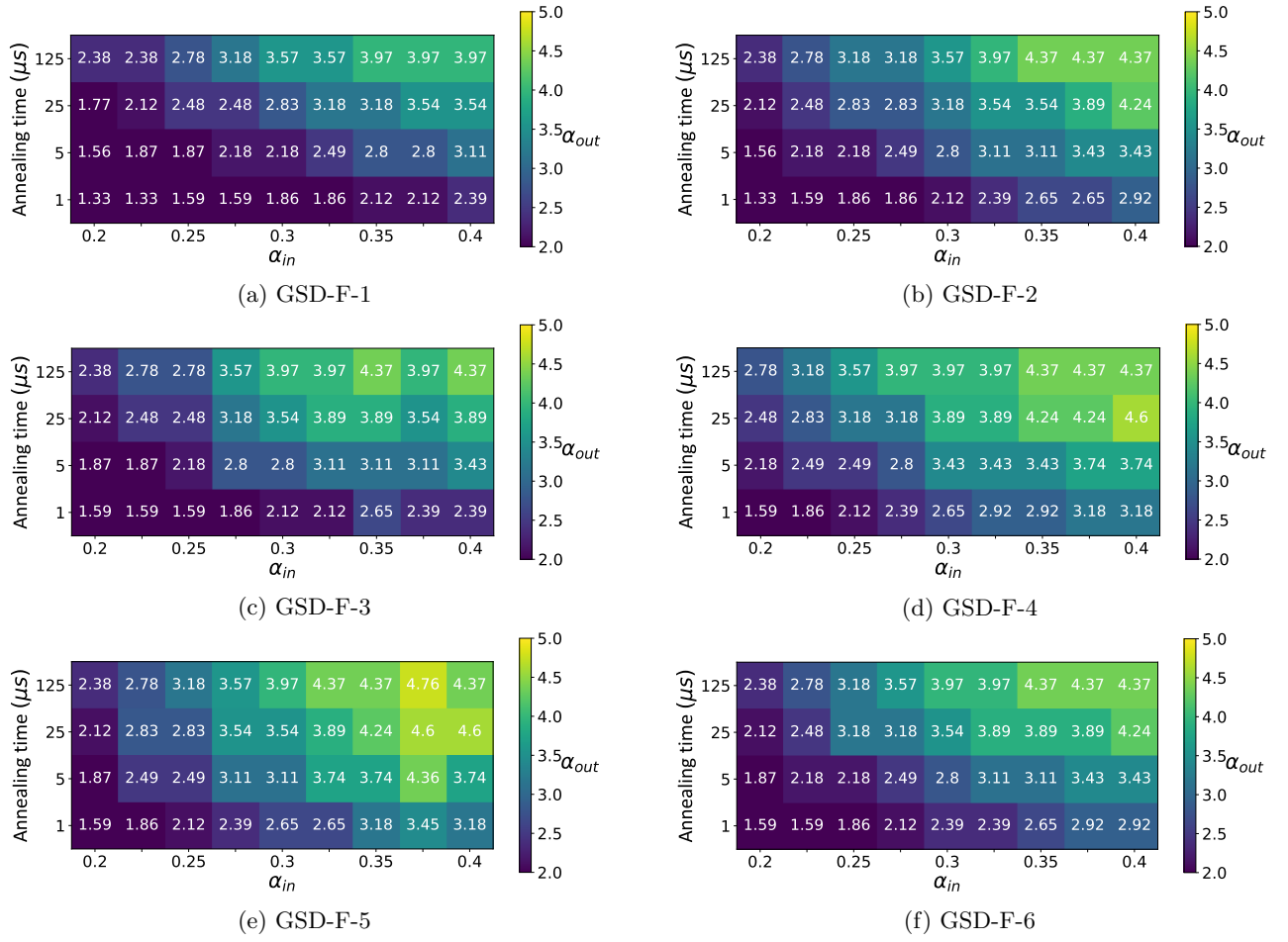


FIG. 12: The dependence of effective temperature α_{out} on α_{in} and annealing time for all GSD-F models.

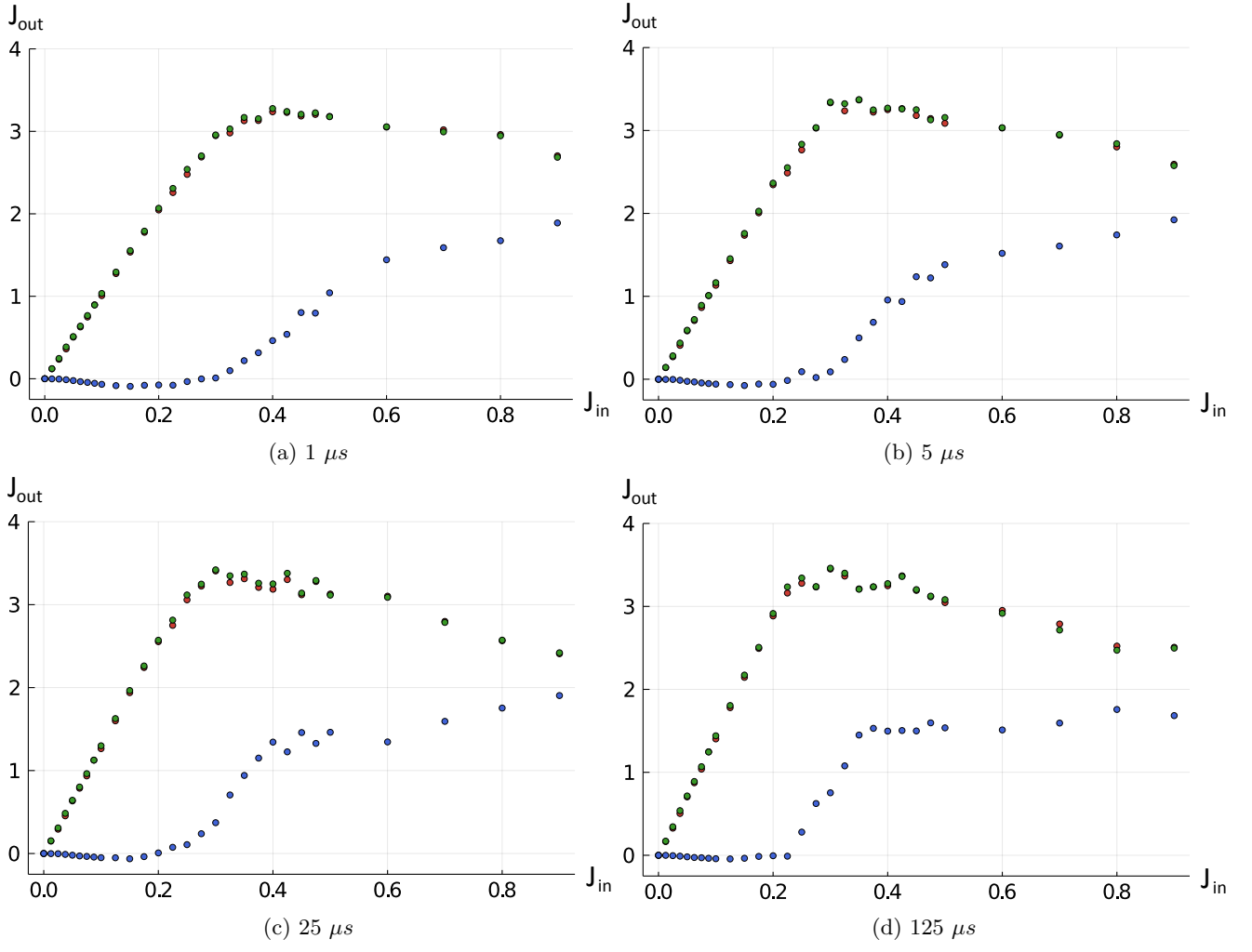


FIG. 13: Three Spin Experiments for Various Annealing Times. Green and red denote the programmed edges J_{12} and J_{23} , respectively. Blue represents the spurious coupling J_{13} .